Fast Magnetic Resonance Spectroscopic Imaging Using RF Coil Arrays

by

Borjan Aleksandar Gagoski

Submitted to the Department of Electrical Engineering and Computer Science

in partial fulfillment of the requirements for the degree of

Master of Science in Electrical Engineering

at the

MASSACHUSETTS INSTITUTE OF TECHNOLOGY

June 2006

Author . . . . . .

Department of Electrical Engineering and Computer Science
May 12, 2006

Certified by. . . . . .

Elfar Adalsteinsson
Robert J. Shillman Assistant Professor of Electrical Engineering and Computer Science; Harvard-MIT Division of Health Science and Technology
Thesis Supervisor

Accepted by . . . . . .

Arthur C. Smith
Chairman, Department Committee on Graduate Students

Fast Magnetic Resonance Spectroscopic Imaging Using RF Coil Arrays

by

Borjan Aleksandar Gagoski

Submitted to the Department of Electrical Engineering and Computer Science
on May 12, 2006, in partial fulfillment of the
requirements for the degree of
Master of Science in Electrical Engineering

Abstract

Conventional Magnetic Resonance Spectroscopic Imaging (MRSI) suffers from both low signal-to-noise (SNR), as well as long acquisition times. The development of high-fidelity gradient coils has opened opportunities for fast k-space encoding schemes that are already used in structural imaging. At the same time, receive-coil arrays using 4 and 23 channels have been developed and reported to produce improved SNR over conventional quadrature detection by single coils. Fast spectroscopic imaging algorithm using spiral k-space trajectories and multiple-channel coil arrays is proposed in order to overcome the long acquisition-time limitations of conventional MRSI.

Thesis Supervisor: Elfar Adalsteinsson

Title: Robert J. Shillman Assistant Professor of Electrical Engineering and Computer Science; Harvard-MIT Division of Health Science and Technology

Acknowledgements

I believe that somebody's success or failure is a pure consequence of the background that s/he comes from and the things/people that s/he encounters. Further, I think that it is not an exaggeration to say that, looking from a greater perspective, one is not to be directly blamed/praised for a failure/success. Rather it is all these "little, unimportant" things that indirectly pave the paths of our lives.

I just got a Master Degree from MIT and *I am to take absolutely no credit for it*. I cannot be more sincere in thanking all of the following for where I am in my life right now.

Elfar, my advisor: the most patient, outgoing and fun professor I've ever known. I still cannot see how he has been managing to calmly explain so many things to me repeatedly, until my stupidity finally gave up. I am thankful for his courage to keep me in his group throughout my rough start as a graduate student here at MIT. I guarantee that there is no "normal-minded' student who will not want him as an advisor: he is an unbelievable expert in the field, the research discussions that we are having are great, and most importantly, he is extremely-super-cool (yes, this is a word) person to be around with.

Litka and Aco, my mom and dad: for being supportive about every single thing that I had in my mind (and off course made sense). They have been with me through thick and thin with all they have. For some reason, they have been having faith in me, even at times when I considerably doubt myself. But I guess parents have the sixth sense, they just know. With the very successful careers that they have, I just wish I could be as successful as they are: as academically smart as my mom and as financially smart as my dad (he is really poor, but that is my and my mom's fault). Уште 8 години до крај на кладбата... губиш тато, губиш.. :).

Karposh, Skopje, Macedonia: the most beautiful neighborhood to grow up in. A tremendous part *of me being Borjan* has a lot to do with: doing stupid things with my friends on the streets (џабалебарење), relax on the local benches and "developing theories" of absolutely no importance (мрчење, фаќање сеир), having great nights singing while the guitar is playing and the wine bottles are continuously opening. It is

funny how every single one *of us* is having a great, successful life. Карпуш 1 и 2 Багро: МАГИСТРИРАВ, шо пие кафана? ;-)

RPI and MIT dudes and girls: the most nerdy (well not all of them), yet great people to be around with. It is with Filipp, Chen, Piotr, Marina, Rokhsana, Joaq, Sahil, AD, Mike (to name a few) that I have been suffering my undergraduate education with, along with the "beauties" of the town of Troy. Then I came to, supposedly the geekest school on earth, and I met all these people who, albeit truly geeky (OK, I will include myself), are great to hang out with. Kawin, Padraig, Joonsung and Joseph could not be better labmates (I won't even start to tell the stories). For Demba, Zahi, Jenn, Bill, Adam ... and the rest of the people from Area I, every comment is insufficient: you have to know them to find out how wonderful people they are.

And off-course the many Balkan's people here in Boston, who I won't even start to name one by one, because of the fear that I will forget somebody: thank you for making me feel more like home while being so far away from it. Also it would be so ungrateful if I don't mention the few relatives that I have here in the States, i.e. Mare, Ivan, Aleks, Igor, Ane and Maja: you have been unbelievably helpful in so many ways during these six years of studying in America.

Thus, I do not really have a master's thesis – all of the above (*and all of those who I deeply regret I didn't mention*) do. It just happened that my name is on the front page.

Great things happen to people who will never forget where they came from, and have great respect to those who have helped them. Honor, pride, honesty and respect are what really matter and Masters/Ph.D. degrees are just things along the way. Thus, I learnt that ...

... in order to be big, you have to remain small.

Massachusetts Institute of Technology, Borjan Gagoski

May, 2006

Table of Contents

1 Introduction ____ *15*

1.1 The chemical shift phenomenon ____ **16**

1.2 Problem Statement and Thesis Structure ____ **18**

2 Conventional vs. Spiral Chemical Shift Imaging ____ *21*

2.1 Challenges in MRSI ____ **22**

2.2 Conventional CSI ____ **23**

2.3 Spiral CSI ____ **26**

2.3.1 Readout in spiral CSI: Temporal and Angular Interleaves ____ 26

2.3.2 Readout part in spiral CSI: Spiral Design ____ 32

2.3.3 Excitation in spiral CSI: The Spectrally and Spatially selective RF pulses ____ 34

2.3.4 Excitation in spiral CSI: The Adiabatic RF pulse ____ 38

3 Spiral CSI Multi Coil Reconstruction ____ *43*

3.1 Calibration Scans ____ **44**

3.1.1 On-resonance frequency drifts ____ 45

3.1.2 Spatial Frequency drifts ____ 46

3.2 Single Coil Reconstruction ____ **50**

3.2.1 The gridding algorithm used in Spiral CSI ____ 51

3.2.2 Improvement of the current gridding algorithm ____ 53

3.2.3 Results from single coil reconstruction ____ 55

3.2.4 Phasing of the reconstructed data ____ 57

3.3 Multi coil reconstruction ____ **59**

3.3.1 Coil sensitivities ____ 60

3.3.2 Results: Spectra and measured SNR ____ 62

3.3.3 Results: Metabolite and Reference maps ____ 65

4 Summary ____ *69*

4.1 Contributions ____ **69**

4.2 Future work ____ **70**

Bibliography ____ *71*

List of Figures

FIGURE 1-1: ^{1}H MR SPECTRUM OF ACETIC ACID (CH_3COOH) SHOWING THE EFFECTS OF THE CHEMICAL SHIFT PHENOMENON. THE COOH GROUP EXPERIENCES DIFFERENT EFFECTIVE B_0 MAGNETIC FIELD COMPARED TO THE CH_3 GROUP. 17

FIGURE 2-1: SPECTRUM FROM A VOXEL LOCATED NEAR A LIPID TISSUE. THE LIPIDS' SIGNAL WAS NOT SUPPRESSED AT ALL. THE SIGNALS OF THE METABOLITES (SHOWN WITH THE ARROW) ARE IN THE NOISE LEVEL, AND THEREFORE THIS SPECTRUM IS USELESS (TI/TE/TR = N\A/288MS/2S; ACQUISITION TIME = 24 SECONDS; 1.5 CM THICK SLICE AND NO ENCODING IN (X,Y); 23

FIGURE 2-2: CONVENTIONAL MRSI. A) TIMING DIAGRAM; B) (k_x, k_y, k_z, k_f) ENCODING. 24

FIGURE 2-3: A TYPICAL SINGLE VOXEL SPECTRUM OF THE HUMAN HEAD. THE ABOVE SPECTRUM IS OBTAINED ON A 1.5T SYSTEM USING CONVENTIONAL MRSI (TI/TE/TR = 171MS/288MS/2S; ACQUISITION TIME = 24 SECONDS; 1.5 CM THICK SLICE AND NO ENCODING IN (X,Y); 24

FIGURE 2-4: A) SPIRAL TRAJECTORIES ARE USED TO ENCODE K_XK_Y PLANE. B) K_Z AXIS IS PHASE ENCODED. ... 27

FIGURE 2-5: SIMULTANEOUS ENCODING ALONG,K_F AXES. EVERY (K_Y,K_Z) POINT IS SEPARATED BY 2.5MS ALONG THE K_F AXIS 28

FIGURE 2-6: ANGULAR (0^0, 90^0, 180^0, 270^0) INTERLEAVES ($N_A = 4$). THE FINAL K-SPACE TRAJECTORY IS FOUR TIMES AS DENSE AS EACH INDIVIDUAL INTERLEAF 29

FIGURE 2-7: TIMING DIAGRAM SHOWING 2 OUT OF THE 4 ANGULAR INTERLEAVES FROM FIGURE 2-6. AFTER THE SCAN IS DONE, THE RAW DATA ARE ASSEMBLED AND RECONSTRUCTED: THE RESULT IS SPECTROSCOPIC DATA ENCODED SPECTRALLY AND SPATIALLY. 30

FIGURE 2-8: TIMING DIAGRAM SHOWING 3 TR PERIODS, EACH OF WHICH PLAYS 3 (OUT OF N_T) TEMPORAL INTERLEAVES. THE LENGTH OF ONE SPIRAL LOBE IS AN INTEGER MULTIPLE OF THE TEMPORAL SAMPLING TIME (UNIFORM TEMPORAL SAMPLING IS OBTAINED) 30

FIGURE 2-9: THE LENGTH OF ONE SPIRAL LOBE IS NOT AN INTEGER MULTIPLE OF THE TEMPORAL SAMPLING TIME AND AS A CONSEQUENCE A NON-UNIFORM TEMPORAL SAMPLING IS OBTAINED. 31

FIGURE 2-10: A) CONSTANT DENSITY K-SPACE SAMPLING, ITS IMPULSE RESPONSE, AND NO WINDOWING USED (ASSUMING FIXED SCAN TIME AND VOXEL SIZE). B) CONSTANT DENSITY K-SPACE SAMPLING, ITS IMPULSE RESPONSE WITH HANNING WINDOW USED. C) VARIABLE DENSITY K-SPACE SAMPLING, ITS IMPULSE RESPONSE WITH HANNING WINDOW USED. 32

FIGURE 2-11: SPATIALLY SELECTIVE RF PULSES. TRAPEZOID GRADIENT IS PLAYED ON THE Z GRADIENT CHANNEL AND A SINC FUNCTION IS PLAYED ON THE RF CHANNEL. THE RESULTANT EXCITED PROFILE IS A RECTANGULAR FUNCTION ALONG THE Z AXIS. 35

FIGURE 2-12: GENERATING A SPECTRAL-SPATIAL RF PULSE. ITS SHAPE IS DETERMINED BY MULTIPLE REPETITIONS (IN TIME) OF THE SPATIALLY-SELECTIVE RF PULSE, MODULATED BY THE SHAPE OF THE FUNCTION RESPONSIBLE FOR THE SPECTRAL SELECTION 36
FIGURE 2-13: SHAPES OF THE REAL PART OF THE SPIN-ECHO SPECTRAL-SPATIAL RF PULSES TOGETHER WITH THE APPROPRIATE GRADIENTS; A) THE 90^0 FLIP RF PULSE; B) THE 180^0 FLIP RF PULSE. 37
FIGURE 2-14: MAGNITUDE AND PHASE PLOTS OF THE INVERSION ADIABATIC PULSE 38
FIGURE 2-15: TIMING DIAGRAM OF THE SEQUENCE USED TO FIND THE RIGHT AMPLITUDE OF THE ADIABATIC INVERSION PULSE. 39
FIGURE 2-16: TESTING THE MAGNITUDE OF THE ADIABATIC PULSE. VERTICAL AXIS REPRESENTS THE MEAN VALUE OF AN AREA WITHIN THE RECONSTRUCTED PHANTOM IMAGE, WHICH GIVES DIRECT MEASURE OF THE LONGITUDINAL MAGNETIZATION, M_Z. THE HORIZONTAL AXIS SHOWS THE PEAK RF VOLTAGE APPLIED TO THE ADIABATIC PULSE. IT CAN BE SEEN THAT ANY VOLTAGE ABOVE 80V GUARANTEES 180^o FLIP OF THE LONGITUDINAL MAGNETIZATION. 40
FIGURE 2-17: TESTING THE TI TIME. THE BLUE, PLOTTING THE PEAK OF THE LIPID AT 1.3PPM AS A FUNCTION OF THE INVERSION TIME, CLEARLY CROSSES ZEROS FOR TI = 172MS, CORRESPONDING TO NULLING THIS PARTICULAR LIPID COMPONENT. TWO SUBJECTS WERE USED TO OBTAINED THE DATA: THE FIRST ONE FOR SCANS WITH TI < 174MS, THE OTHER FOR SCANS WITH TI > 172. AFTER THE SCANS WERE DONE, THE DATA WAS COMBINED TO OBTAIN THE ABOVE PLOT. 41
FIGURE 3-1: CHECKING FOR ON-RESONANCE FREQUENCY DRIFTS: A) THE 11 SPECTRA FROM THE FREQUENCY NAVIGATORS OF A REFERENCE (4 MINUTE) SCAN ARE OVER PLOTTED ONE ON TOP OF ANOTHER. DIFFERENT COLOR CORRESPOND TO SPECTRUM FROM A DIFFERENT NAVIGATOR; B) THE BOX SELECTED IN A) ZOOMED IN: THIS VERIFIES THAT THE FREQUENCY DOESN'T DRIFT THROUGHOUT THE SCAN. 45
FIGURE 3-2: IN PLANE RAW DATA FOR TWO ANGULAR INTERLEAVES OF THE SPIRAL LOBE JUST BEFORE THE EFFECTIVE SPIN ECHO. IN THE GRAPHS ABOVE, TE WAS TUNED TO HAPPEN RIGHT AFTER: A) 2 SPIRAL LOBES; B) 6 SPIRAL LOBES; C) 10 SPIRAL LOBES; D) 14 SPIRAL LOBES; 48
FIGURE 3-3: DETERMINING THE EFFECT OF THE SPATIAL FREQUENCY DRIFTS RECORDED BY FEEDING THE RECONSTRUCTION ROUTINE WITH SYNTHESIZED RAW DATA OF A LARGE-FOV OBJECT; A) RECONSTRUCTION RESULTS USING THE ORIGINAL K-SPACE TRAJECTORY. B) RECONSTRUCTION RESULTS USING MODIFIED K-SPACE TRAJECTORY THAT REFLECTS THE NUMERICAL VALUES OF THE SPATIAL FREQUENCY DRIFTS FROM TABLE 1. THE DIP THAT CAN BE SEEN IN THE MIDDLE OF THE IMAGE IS ABOUT 1.2% LOWER THAN THE MAXIMUM VALUE. 49
FIGURE 3-4: SCHEMATIC EXPLANATION OF THE IMPROVEMENT OF THE GRIDDING ALGORITHM BASED ON THE FACT THAT SAMPLES ALONG K_F AXIS ARE SAMPLED UNIFORMLY. AFTER APPROPRIATELY REARRANGING THE SAMPLES FROM ALL THE TEMPORAL AND ANGULAR INTERLEAVES, THEY ARE APPROPRIATELY PHASED AND FFT ALONG THE K_F AXIS IS PERFORMED. THE RESULTING (K_X, K_Y, F) MATRIX IS GRIDDED ALONG K_X AND K_Y AXIS ONLY, TO OBTAIN THE DESIRED (X,Y,F) DATA. 54

FIGURE 3-5: IMAGE DATA OVER ALL FREQUENCIES, REFERENCE SPECTRUM AND METABOLITE SPECTRUM AT (X=32,Y=32) OBTAINED FROM: A) 3D GRIDDING RECONSTRUCTION; B) 1D FFT ALONG K_F AXIS FOLLOWED BY 2D GRIDDING ALONG K_X AND K_Y DIRECTIONS. 55

FIGURE 3-6: RESULTS FROM RECONSTRUCTION THE DATA FROM SINGLE COIL ACQUISITION. REAL PARTS OF THE SPECTRA (ALL SHOWN ON THE SAME SCALE) FROM THE 16^{TH} AND 17^{TH} SLICE, AT NINE SPATIAL LOCATIONS WITHIN THE SPECIFIED BOX ARE SHOWN. TI/TE/TR=N/A/288MS/2S. 56

FIGURE 3-7: RECONSTRUCTED GRE PROFILES (LEFT-HAND SIDE) AND THEIR LLSE ESTIMATE (RIGHT-HAND SIDE) FOR THE 17^{TH} SLICE (MAGNITUDE PLOTS); A) 4-CHANNEL COIL ARRAY; B) 23-CHANNEL COIL ARRAY. THE NUMBERS ABOVE EACH IMAGE REPRESENT THE ABSOLUTE SCALING OF THE PROFILE RELATIVE TO THE REST OF THE PROFILES. FOR EXAMPLE, IN B) THE MAXIMUM VALUE AMONG ALL THE PROFILES IS IN THE 12^{TH} COIL, WHICH IS TWICE AS LARGE AS THE MAXIMUM VALUE IN THE 22^{ND} COIL. 61

FIGURE 3-8: RESULTS FROM RECONSTRUCTION THE COMBINED DATA FROM 4-CHANNEL COIL ARRAY ACQUISITION. REAL PARTS OF THE SPECTRA (ALL SHOWN ON THE SAME SCALE) FROM THE 16^{TH} AND 17^{TH} SLICE, AT NINE SPATIAL LOCATIONS WITHIN THE SPECIFIED BOX ARE SHOWN. TI/TE/TR=N/A/288MS/2S 62

FIGURE 3-9: RESULTS FROM RECONSTRUCTION THE COMBINED DATA FROM 23-CHANNEL COIL ARRAY ACQUISITION. REAL PARTS OF THE SPECTRA (ALL SHOWN ON THE SAME SCALE) FROM THE 16^{TH} AND 17^{TH} SLICE, AT NINE SPATIAL LOCATIONS WITHIN THE SPECIFIED BOX ARE SHOWN. TI/TE/TR=N/A/288MS/2S 63

FIGURE 3-10: NAA, CRE, CHO AND ON-RESONANCE (WATER) MAPS FROM A 3D VOLUMETRIC 4-CHANNEL ACQUISITION. THE FIRST THREE ARE OBTAINED FROM THE 15 MINUTES METABOLITE SCANS, WHEREAS THE LAST ONE IS OBTAINED FROM THE 4 MINUTES REFERENCE SCAN. THE NUMBERS SHOWN REPRESENT THE ABSOLUTE SCALING OF A MAP RELATIVE TO THE REST OF THE MAPS. 66

FIGURE 3-11: NAA, CRE, CHO AND ON-RESONANCE (WATER) MAPS FROM A 3D VOLUMETRIC 23-CHANNEL ACQUISITION. THE FIRST THREE ARE OBTAINED FROM THE 15 MINUTES METABOLITE SCANS, WHEREAS THE LAST ONE IS OBTAINED FROM THE 4 MINUTES REFERENCE SCAN. THE NUMBERS SHOWN REPRESENT THE ABSOLUTE SCALING OF A MAP RELATIVE TO THE REST OF THE MAPS. 67

List of Tables

TABLE 1: PEAK SIGNAL VALUES AND THEIR (KX,KY)-SPACE LOCATION FOR DIFFERENT VALUES OF TE..... 47
TABLE 2: SNR MEASURES FROM THE SPECTRA SHOWN ON FIGURE 3-6 56
TABLE 3: SNR VALUES FOR THE SPECTRA SHOWN IN FIGURE 3-8. 63
TABLE 4: SNR VALUES FOR THE SPECTRA SHOWN IN FIGURE 3-9 64
TABLE 5: SNR RATIOS BETWEEN THE SINGLE AND 4-CHANNEL RECONSTRUCTION. THE VALUE IN THIS TABLE FOR A SPECIFIC SPATIAL LOCATION IS OBTAINED BY DIVIDING THE SNR MEASURES IN TABLE 3 BY THOSE IN TABLE 2. 64

1 Introduction

Based on the Nuclear Magnetic Resonance (NMR) phenomenon discovered by Bloch [1] and Purcell [2] independently in 1946, it was not until 1973 that Magnetic Resonance Imaging (MRI) started to gain more attention; this year, Lauterbur [3] demonstrated that molecules put in a strong magnetic field can be spatially mapped using linear gradient fields. Since then, great improvement has been made both in hardware and software, making MRI one of the most powerful imaging techniques used in many scientific areas, especially in medicine for the purpose of diagnosing. The qualitative information (structural and anatomical) embedded in these images, in many cases, proves to be better than that using other imaging techniques (e.g. Computer Tomography, etc).

The work presented in this thesis is in the area of Magnetic Resonance Spectroscopic Imaging (MRSI), and therefore all the topics discussed are closely related to this field of MRI. MRI technology has grown so rapidly and so immensely, that it is not possible to cover all the MRI basics as a part of a master's thesis. Well-written, detailed discussions of various topics, including the fundamentals of MRI, is given in [4-7] and the reader should refer to these books to learn more about MRI in general. Due to their clear and unambiguous discussions, material from [5, 7] in particular was used as a guideline in several sections in this thesis.

This introduction chapter will give a brief overview of the chemical shift phenomenon which is the basis for MRSI. For a more detailed and thorough description one should refer to the appropriate chapters in [5, 7]. At the end of this chapter I will give a brief problem statement and an overview of the organizational structure in which the material in this thesis is presented.

1.1 The chemical shift phenomenon

MRI is a great tool not only because it enables informative structural imaging, but also due to the fact that it offers possibilities for monitoring biochemistry *in vivo*. MRSI, also known as chemical shift imaging (CSI), is an imaging technique where one obtains a spectrum of the signals, e.g. brain metabolites *in vivo*, from an isolated volume of tissue. MRSI is based on the MR phenomenon of chemical shift, a subtle frequency shift in the signal that is dependent on the chemical environment of the particular compound. It is due to this frequency shift that there is a potential for physiological evaluation and material characterization of a volume of interest.

Chemical shift is defined as a small displacement of the resonance frequency due to shielding created by the orbital motion of the surrounding electrons in response to the main B_0 field. By placing a sample of biological tissue in a uniform magnet, exciting it, recording its free induction decay (FID), and then Fourier transforming the FID, the resultant MR spectrum shows resonances at different frequencies corresponding to different chemical shifts. The amount of displacement and the amplitude of the peaks in the spectrum depend on the molecular structure of the compound of interest. Being in a presence of B_0, the effective field experienced by the nucleus is $B_{eff} = B_0 - B_{0\sigma}$. Further, bearing in mind that ω is proportional to B_0 (the Larmor relationship), we have that

$$\omega_{eff} = \omega_0 - \omega_{0\sigma} = \omega_0(1-\sigma) \tag{1.1}$$

where σ equals the shielding constant that depends on the chemical environment, and therefore $\omega_{0\sigma}$ is the displacement of the resonance frequency. From this, it can be concluded that *the change in frequency is proportional to the strength of the main magnetic field* B_0.

The frequency axis in MRSI, for historical reasons, is such that the frequency decreases from left to right and it's given in units of "parts per million" or p.p.m. The chemical shift is defined with respect to a reference frequency ω_r. If the resonance frequency of the sample of interest is ω_s, the chemical shift δ, in p.p.m units (using (1.1)) is:

$$\delta = \frac{\omega_s - \omega_r}{\omega_r} \cdot 10^6 = \frac{\omega_0(1-\sigma_s) - \omega_0(1-\sigma_r)}{\omega_0(1-\sigma_r)} \cdot 10^6 = \frac{\sigma_r - \sigma_s}{1-\sigma_r} \cdot 10^6 \approx \boxed{(\sigma_r - \sigma_s) \cdot 10^6} \quad (1.2)$$

where the last approximation is due to the fact that $\sigma_r \ll 1$.

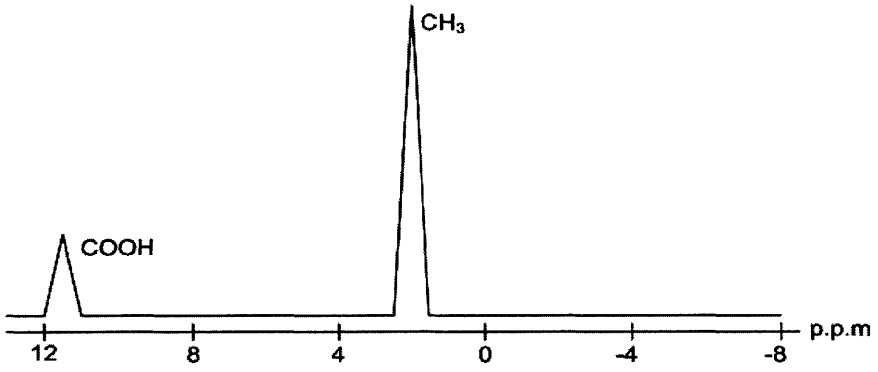

Figure 1-1: ^{1}H MR spectrum of acetic acid (CH_3COOH) showing the effects of the chemical shift phenomenon. The COOH group experiences different effective B_0 magnetic field compared to the CH_3 group.

A schematic ^1H spectrum is given in Figure 1-1. Due to the fact that the valency of the oxygen in the COOH group leads to an attraction of the electron away from the proton, there is less shielding for the proton in the COOH group compared to the proton in the CH_3 group. This is why COOH deviates more from the reference frequency (positioned at 0 p.p.m), compared to CH_3.

The work done in this thesis is dedicated on obtaining ^1H spectra of the human head, meaning that the spectra presented in the subsequent chapters span frequency bandwidth in the neighborhood of the resonance frequency of hydrogen (i.e. water). However, it is worth mentioning that ^{13}C and ^{31}P CSI is of significant importance. For example, ^{31}P spectra are used for obtaining quantitative information about chemical compounds like adenosine triphosphate (ATP), phosphocreatine (PCr), and inorganic phosphate (P_I). However, it is worth mentioning that ^{13}C and ^{31}P spectra have significantly lower signal-to-noise ratio (SNR) compared to ^1H spectra and therefore are more difficult to detect and quantify. This is mainly because of lower abundance and sensitivity for these nuclei.

1.2 Problem Statement and Thesis Structure

Conventional in vivo CSI scans suffer from intrinsically low SNR signal and long acquisition times. The main objective of the work in this thesis is to implement and develop algorithm for fast spectroscopic imaging which will reduce the acquisition times and have comparable SNR measures as the conventional CSI scans. The spiral CSI algorithm developed by [8] was used in order to achieve this objective.

The contributions of this thesis include:

- Implementation of the Spiral CSI algorithm on a commercial, clinical Siemens MRI platform.
- Reconstruction of volumetric spectroscopic data acquired from multi-coil RF arrays in order to increase the SNR.
- Improved efficiency of the reconstruction algorithm used in [8].

The material provided in this thesis involves:

- Definition and elaboration of the spiral CSI algorithm including its advantages and disadvantages.
- Explanation of the reconstruction algorithm.
- Presentation and evaluation of the results obtained from reconstructing the acquired, single and multi-coil, spectroscopic data.
- Discussion of issues encountered in various calibration and testing stages in the process of implementing the spiral CSI algorithm.

The above material is covered in two chapters. The second chapter in the thesis entitled "Conventional vs. Spiral Chemical Shift Imaging" starts by giving the derivation of the signal equation for the case of spectroscopic imaging. It continues with discussion on the general challenges faced in CSI and gives a brief overview of the conventional CSI algorithm, where its main disadvantages are revealed. Proposal of a way to overcome these disadvantages leads to the spiral CSI algorithm which is then defined and thoroughly analyzed. This discussion is divided into two parts: the first one talks about the readout part of the spiral CSI algorithm (including temporal and angular interleaves, spiral designs etc); the second talks about the excitation part (including the design of the adiabatic and spectral-spatial spin-echo RF pulses).

Having explained the theory behind the spiral CSI algorithm, the third chapter entitled "Spiral CSI Multi Coil Reconstruction" deals with the process of reconstructing the acquired spectroscopic data. At the outset of this chapter, I give a brief introduction of the overall process of acquiring all the raw data files from the Siemens 1.5T scanner, which will later be fed to the MATLAB and C++ programs so that the reconstruction can take place. After that, I spend several sections discussing issues regarding spatial and on-resonance frequency drifts, as well as appropriate data phasing routines. This is followed by explanation of the single coil reconstruction algorithm, touching mainly upon the gridding routine. Discussion on the latter leads to an idea that excludes gridding along one dimension, thus increasing the efficiency of the overall reconstruction process without any loss in the quality of reconstructed data.

Finally, results from 1-, 4- and 23-coil acquisitions from normal volunteers in vivo are presented and analyzed. This involves figures of spectra from specific spatial locations of the reconstructed data, together with plots of metabolite and water-reference maps, as well as plots of the coil profiles used in combing the reconstructed data from different coils. Finally, quantitative SNR measures are presented for the single- and multi-coil reconstructed data, concluding that using multiple coils for data acquisition yields SNR increase.

The last chapter, entitled "Conclusion and future work" gives a comprehensive summary of what has been accomplished, again emphasizing the contributions of the work presented in this thesis. This is followed by mentioning several possible applications that the spiral CSI algorithm can be of great usage: 2D spectroscopy or CSI on higher main field strengths (3T, 7T systems etc). In addition, future projects might also include further acquisition time improvement by implementing Parallel CSI or additional novel Fourier domain sampling schemes.

2 Conventional vs. Spiral Chemical Shift Imaging

In what follows I give a qualitative comparison between conventional phase-encoded and spiral chemical-shift imaging (CSI). At the end of the chapter I expect that the reader will appreciate the idea behind spiral CSI: trading temporal sampling for efficient spatial k-space sampling leading to a reduction in the scan time without loss in SNR per unit time compared to conventional CSI.

Before giving brief overview of the conventional CSI and laying down its advantages and disadvantages together with the motivation for improvement (that would lead to the spiral CSI algorithm), it is instructive to review the derivation of the signal equation for the case of spectroscopic imaging. The derivation presented followed closely that of Dwight Nishimura [7].

Leaving out the frequency axis for the time being, and considering only a three-dimensional (3D) space of interest, one can imagine a tiny "magnetic oscillator" rotating at frequency $\omega = \gamma \cdot B$ (γ is the gyromagnetic ratio and B is the main magnetic field) at each spatial location (x, y, z). Modeling these magnetic oscillators as having (constant in time) magnitude $m(x, y, z)$ and (variable in time) phase $\phi(x, y, z, t)$, the signal seen by the receive coils, i.e. the transverse magnetization, is given by

$$s(t) = \int_x \int_y \int_z m(x, y, z) \cdot e^{-i\phi(x,y,z,t)} dxdydz \tag{2.3}$$

Bearing in mind that frequency is the time rate of change in phase, and that it is proportional to the applied field $B(x, y, z, t)$, one can write the following:

$$\phi(x,y,z,t) = \int_0^t \frac{d}{dt}\phi(x,y,z,\tau)\,d\tau = \int_0^t \omega(x,y,z,\tau)\,d\tau = \gamma \int_0^t B(x,y,z,\tau)\,d\tau \quad (2.4)$$

knowing that $B(x,y,z,t) = B_0 + G_x(t)\,x + G_y(t)\,y + G_z(t)\,z$ and that k-space is defined as the time integral of the gradients, i.e.

$$k(t) = \frac{\gamma}{2\pi} \int_0^t G(\tau)\,d\tau, \quad (2.5)$$

the signal equation given in (2.3) becomes

$$s(t) = \int_x \int_y \int_z m(x,y,z) \cdot e^{-i[k_x(t)\,x + k_y(t)\,y + k_z(t)\,z]}\,dxdydz \quad (2.6)$$

The difference between (2.6) and the signal equation in MRSI, is the consideration of a frequency axis in order to account for the chemical shift phenomenon. Therefore, defining $k_f(t) = t$, the signal equation in MRSI becomes

$$s(t) = \int_x \int_y \int_z \int_f m(x,y,z,f) \cdot e^{-i[k_x(t)\,x + k_y(t)\,y + k_z(t)\,z + k_f(t)\,f]}\,dxdydzdf \quad (2.7)$$

Equation (2.7) is a four-dimensional (4D) Fourier Transform (FT) of the excited object and its spectral contents. From this, it is clear that the inclusion of the temporal variable adds another dimension to the imaging problem compared to structural imaging. This formulation clearly depicts volumetric CSI acquisition and reconstruction as a four-dimensional sampling problem.

2.1 Challenges in MRSI

The main constraint in MRSI comes from the fact that the signals of the metabolites that we are interested in are orders of magnitude lower compared to the signals coming from the water and the lipids. The concentration of the water molecules is approximately 55 M, and those of the metabolites of interest are less than 10 mM [9]. This fact is the main reason why MRSI scans have intrinsically low SNR compared to conventional MRI of water. Figure 2-1 shows that compared to subcutaneous fat signals near the brain, the metabolite spectra are much lower and present a large dynamic range between the desired metabolites and the artifact signals from fat.

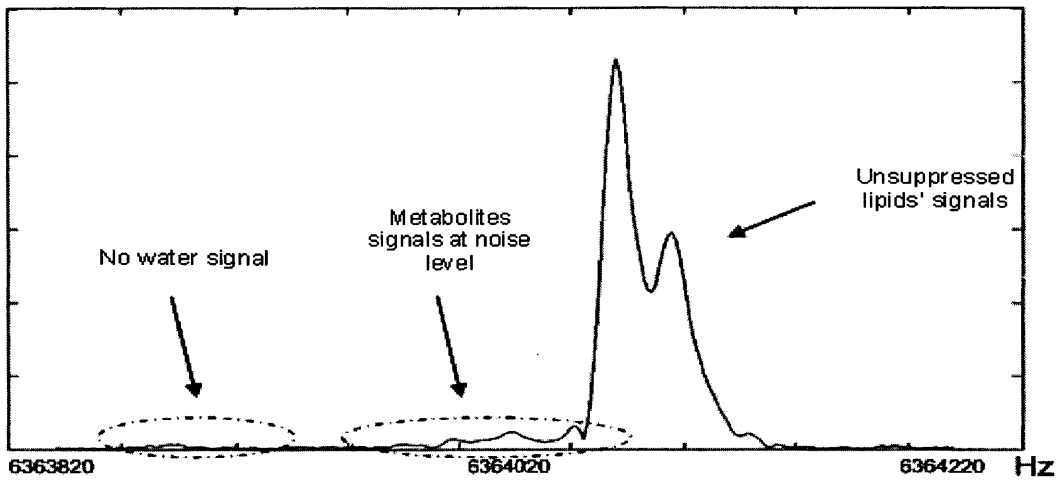

Figure 2-1: Spectrum from a voxel located near a lipid tissue. The lipids' signal was not suppressed at all. The signals of the metabolites (shown with the arrow) are in the noise level, and therefore this spectrum is useless (TI/TE/TR = N\A/288ms/2s; Acquisition time = 24 seconds; 1.5 cm thick slice and no encoding in (x,y);

Furthermore, main field inhomogeneities may additionally lower the SNR in MRSI and complicate signal detection and quantification. Any undesirable variations in the main magnetic field B_0 will cause a shift along the frequency axis, causing overlap of the metabolites' peaks and creating ambiguity in metabolites' identification. These main field inhomogeneities are mainly due to susceptibility effects within the body near the boundaries of air and tissue, and thus vary from one subject to another.

2.2 Conventional CSI

A straightforward way of doing spectroscopic imaging is to do the following (in order, and per repetition time, TR) [10, 11]: excite the volume of interest, "travel" to a certain (k_x, k_y, k_z) position by applying short gradient lobes of appropriate area and "stop", turn the Analog to Digital Converter (ADC) on, and finally, record the free induction decay signal (FID). This is to be repeated for all (k_x, k_y, k_z) locations of interest. The number of repetition times will depend on the Field of View (FOV) and the spatial resolution requirements. This is pictorial depicted in Figure 2-2.

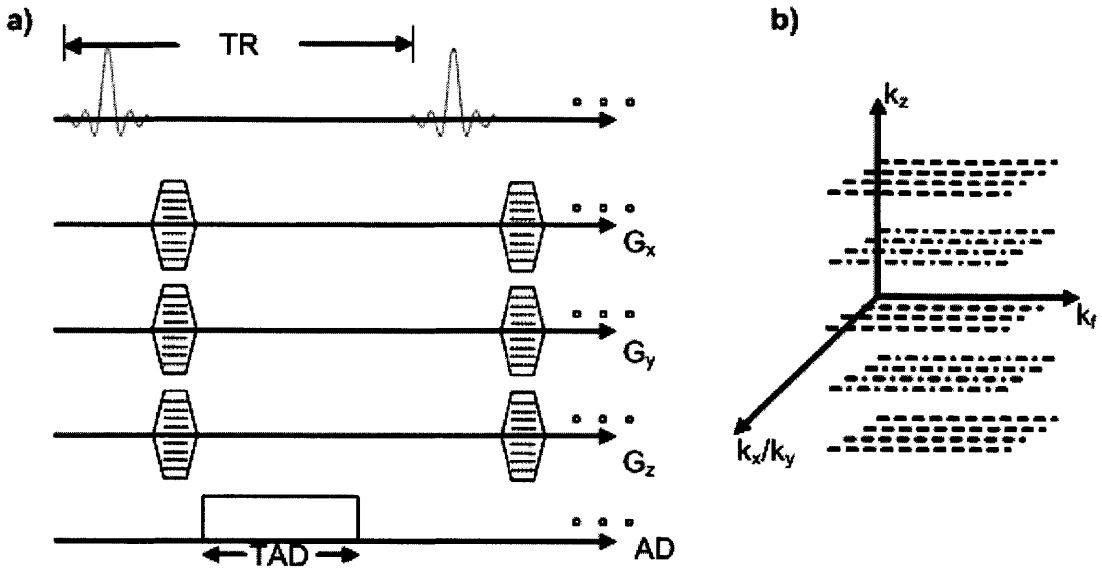

Figure 2-2: Conventional MRSI. a) timing diagram; b) (k_x, k_y, k_z, k_f) encoding.

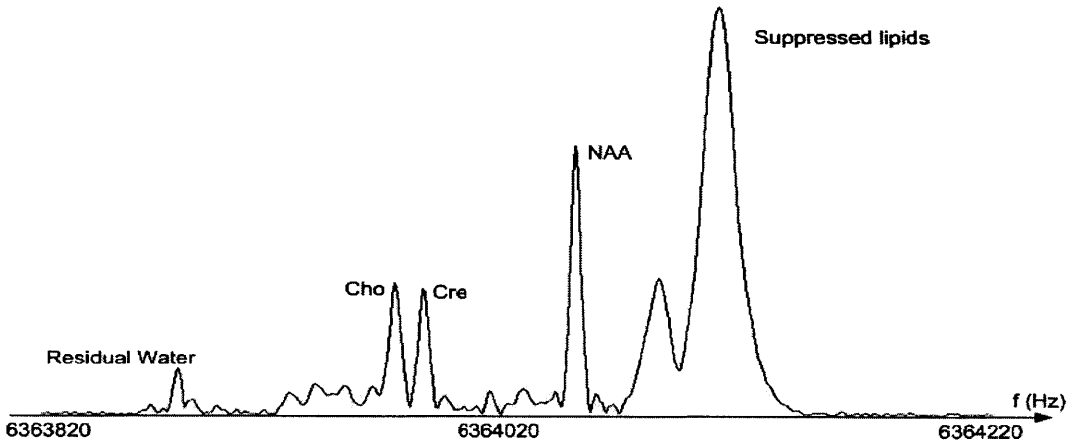

Figure 2-3: A typical single voxel spectrum of the human head. The above spectrum is obtained on a 1.5T system using conventional MRSI (TI/TE/TR = 171ms/288ms/2s; Acquisition time = 24 seconds; 1.5 cm thick slice and no encoding in (x,y);

A typical single voxel spectrum is given in Figure 2-3. In this figure it is clear that the water and lipid signals have been significantly suppressed. In order to suppress the water signal, spectrally selective RF pulses [12] (a spin-echo pair) are used in this particular sequence design. These pulses act like band-pass filter along the k_f axis: the frequency of the water signal is in their stop band, but the frequencies of the lipid signal

are in their pass band mainly because the lipid signals and the metabolites signals are spectrally close. In this method, to suppress the lipid signal, adiabatic inversion pulse is used, which, if used with the correct inversion time (TI) for the lipids, it nulls the signals for one T1 species. The spectral-spatial RF and adiabatic pulse pulses will be discussed in more details in sections 2.3.3 and 2.3.4 respectively.

As mentioned, MRSI suffers from intrinsically low SNR. Since SNR in MRI is proportional to the acquisition time and the voxel size [13, 14], i.e.

$$SNR \propto V_{size} \cdot \sqrt{T_{AD}}, \tag{2.8}$$

in order to improve SNR, one could increase the voxel volume, or acquisition time, or both. Moreover, voxel size depends on the spatial resolution (lower spatial resolution gives larger voxel size), and further, the number of (k_x, k_y, k_z) encodes depends on the FOV and spatial resolution parameter. Having said this, it can be concluded that *FOV, spatial resolution and imaging time are not independent parameters in conventional MRSI*. This is the main reason for one of the biggest disadvantages in conventional MRSI – the inflexible coupling between scan time and resolution parameters. As an example, a volumetric scan that encodes a volume at a modest 16^3 k-space locations with $TR = 2s$ takes about 2 hours and 20 minutes, a prohibitive scan time for in vivo exams.

The hardware of the gradients has undergone major improvements in recent years, allowing possibilities for very fast k-space traversing. Nevertheless, the conventional MRSI takes absolutely no advantage of the gradients' potential, suggesting that efficient k-space sampling with time-varying gradients as a method to overcome the rigid constraints on minimum acquisition time in phase-encoded MRSI. In addition, looking at (2.8) it can be seen that *the SNR does not depend on the number of voxels.* This latter fact, together with fast k-space sampling, provides the basis for the development of a fast MRSI algorithm using time-varying gradients. Many authors have touched upon the theory and application of applying time-varying gradients during the readout of a spectroscopic acquisition [15-26]. A comprehensive *in vivo* implementation of fast CSI algorithm that is based on spiral k-space trajectories was done by [8, 27] (Adalsteinsson et al.) The work presented in these papers is the core of this thesis' work, and therefore complete understanding of this algorithm is critical. The rest of this chapter is dedicated to explanation of the design and implementation of the spiral CSI algorithm.

2.3 Spiral CSI

In conventional CSI, spectral bandwidth is said to be "free" since the ADC design on the current (Siemens) MRI systems allows temporal sampling of as low as $1\mu s$, corresponding to very wide spectral bandwidth of $1MHz$. However, on 1.5 Tesla systems, the metabolites of interests span frequencies that are within a spectral range of $400Hz$. This implies that $400Hz$, corresponding to temporal sampling of $2.5ms$, is a sufficient spectral bandwidth for the purposes of MRSI – temporal sampling at less than $2.5ms$ per point is not logical since it does not provide any more information about the proton metabolites of interest.

This fact opens the doors for the development of a CSI algorithm that is more efficient than the phase encoded CSI scheme. As a matter of fact, "traveling" to a certain k-space location and then turning on the ADC just to acquire data for the fourth, k_f, direction is sub-optimal with respect to sampling efficiency of multi-dimensional k-space, as one would immediately argue that within those $2.5ms$ (which we agreed is the sufficient sampling time), more than one k-space sample can be acquired. Furthermore, as noted in the previous section and in [13, 14], SNR is independent of the number of voxels, so acquiring as many k-space samples as possible within the sampling time, will not lower the SNR, provided that the reconstruction algorithm is properly designed. This idea is the backbone of all CSI encoding methods with time-varying gradients [15-26], and among those, spiral-based k-space trajectories make excellent use of available gradient amplitude and slew rate.

In what follows, the spiral CSI acquisition for proton spectroscopic imaging is going to be explained in two parts: 1. Readout part, which deals with the design of the spiral trajectories; and 2. Excitation part, which deals with the design of the spectral-spatial RF pulses (used as a spin-echo pair) and the Adiabatic (Inversion) RF pulse.

2.3.1 Readout in spiral CSI: Temporal and Angular Interleaves

The primary constraint of the sampling requirements is that different samples of the same (k_x, k_y, k_z) point need to be separated by no more than $2.5ms$ on the k_f axis. The common practice to use bigger voxel sizes in MRSI for the purposes of improving the

SNR goes in favor of the spiral CSI algorithm, since for a given FOV, one does not have to acquire samples at high spatial frequencies, inherently reducing the number of required k-space samples.

Nevertheless, it is almost always impossible to traverse certain k-space volume in only $2.5ms$ given the spatial resolution and FOV constraints. In order to simplify this problem, the current spiral CSI algorithm does not implement spiral trajectories that traverse a 3D (k_x,k_y,k_z) volume. Instead, the k_z axis is phase encoded, so that 2D spiral trajectories are played on the k_xk_y plane at each value of k_z. This is shown on Figure 2-4. Therefore, in the rest of this chapter we are only going to discuss and comment on spectroscopic data that is encoded in (k_x,k_y,k_f), since going to (k_x,k_y,k_z,k_f) is straightforward.

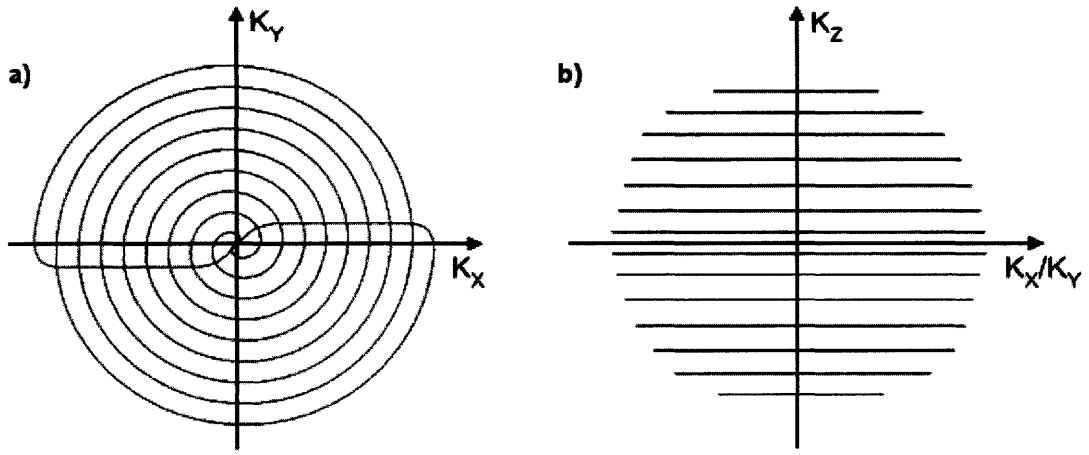

Figure 2-4: a) Spiral trajectories are used to encode k_xk_y plane. b) k_z axis is phase encoded.

For small objects, sometimes it is possible to traverse the k-space plane of interest within $2.5ms$. The reason is that the FOV is small, and therefore the spirals to be played out need to sample k-space rather sparsely (k-space sampling is inversely proportional to the spatial FOV), requiring less sample points (and therefore less time). This idea is shown in

Figure 2-5. Having said that, exciting a thin plane of interest, playing the designed spiral trajectory repeatedly in rather long readout time (let's say $400ms$, corresponding to $400ms/2.5ms=160$ k_f samples) will give us a spectroscopic data, (both spatially and spectrally encoded) in only one TR period! (Note that this data is going to have low SNR,

so perhaps averaging needs to be done. The point here however, is to show that meaningful spectroscopic data is possible to be obtained even in, as short as, one TR period).

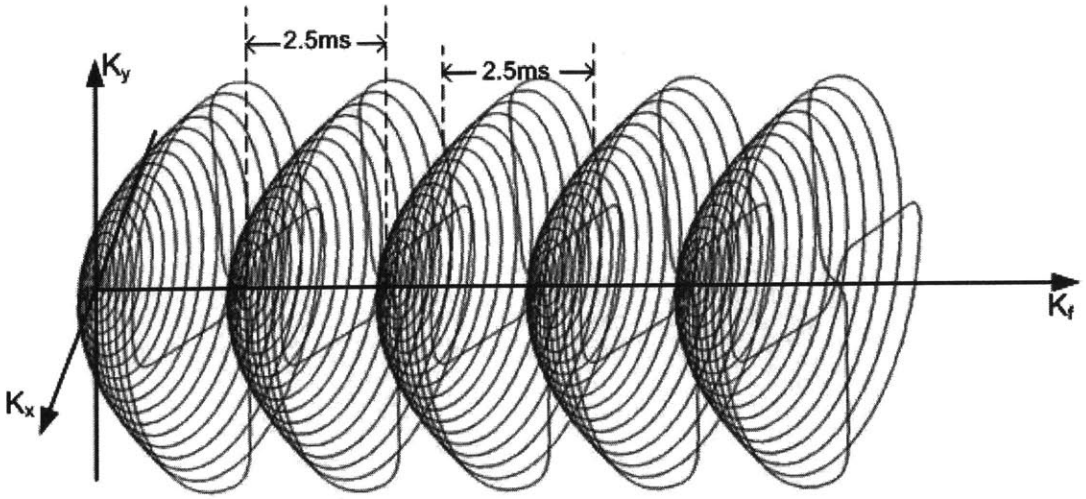

Figure 2-5: Simultaneous encoding along,k_f axes. Every (k_y,k_z) point is separated by 2.5ms along the k_f axis

However, when doing human brain MRSI, the spatial FOV is on the order of 20 cm, so typically it is still impossible to traverse the $k_x k_y$ plane in $2.5ms$ with clinical gradient hardware. In order to overcome this problem, two kinds of spiral interleaves are used: *angular* and *temporal* interleaves.

With angular interleaves, commonly used in spiral MRI, the desired k-space spiral trajectory is divided, or decomposed into spiral trajectories (angular interleaves) that are sparser than the original one. The reason for this decomposition is obvious: each interleaf will have less samples than the original spiral, and thus take less time. If used individually to reconstruct the data, these interleaves would produce data that consist of spectra of spatially aliased image due to violation of the FOV constraint.

One way of decomposing a spiral trajectory (and the one that is used in spiral CSI) is given in Figure 2-6. Let's start with a sparsely sampled spiral interleave. If one takes this interleave, rotate it for 180° (hence the name angular interleaves), and then put it on k-space plane together with the original interleave, what is going to be obtained is spiral trajectory that samples k-space twice as dense as the original interleave. Moreover, rotations of, let's say 60^0, 120^0, 180^0, 240^0 and 300^0 degrees will give spiral

trajectory that is six times as dense as the original interleave. Following this pattern, given a spiral trajectory, one can easily decompose it into N_A different angular interleaves. The number N_A depends on the spiral trajectory to be decomposed and the sampling time along the k_f axis. One can easily observe that if each of the angular interleaves is made such that it takes at most $2.5ms$, obtaining spectroscopic data will take N_A TR periods. Figure 2-7 shows this pictorially.

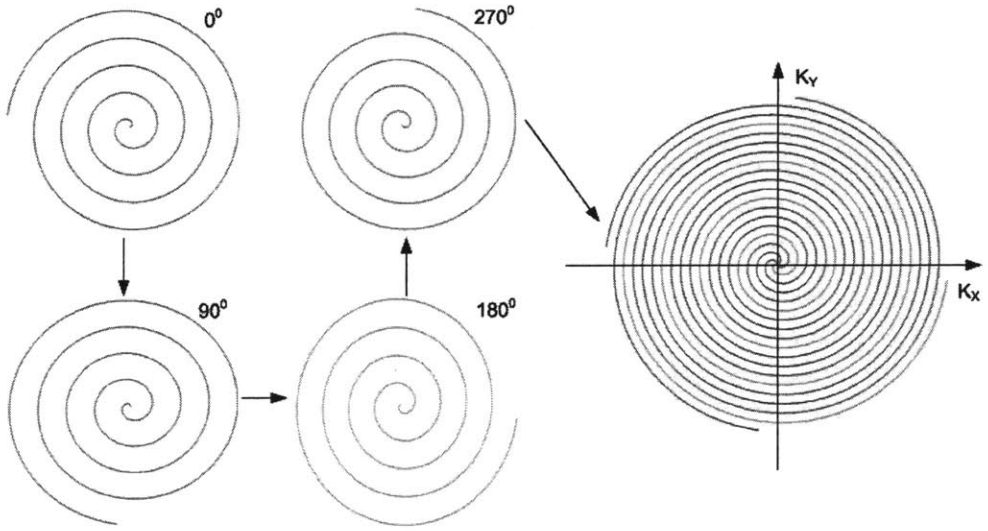

Figure 2-6: Angular (0^0, 90^0, 180^0, 270^0) interleaves (N_A = 4). The final k-space trajectory is four times as dense as each individual interleaf.

Although angular interleaves alone can be used to satisfy gradient constraints and sampling requirements, they are not the only way to implement spiral CSI. A second type of interleaving that produces the same overall result is to use temporal interleaves. In this case, temporal interleaves are implemented by simply shifting the original spiral trajectories along the k_f axis by the critical temporal sampling time (in this case $2.5ms$). For example, let's assume that one period of the original spiral trajectory that fulfills the FOV and spatial resolution requirements takes $7.5ms$. During a given acquisition time, certain (integer) number of these lobes can be played repeatedly. On subsequent TR, the starting time of the spiral lobes is $2.5ms$ later. Note that the ADC is turned on at the same time as before, meaning that the Fourier domain data won't contain spatially informative data from the samples in the first $2.5ms$. Further, on the third TR, the spirals

are going to be shifted $2.5ms$ later relative to those in the second TR ($5.0ms$ relative to the first TR), and so on.

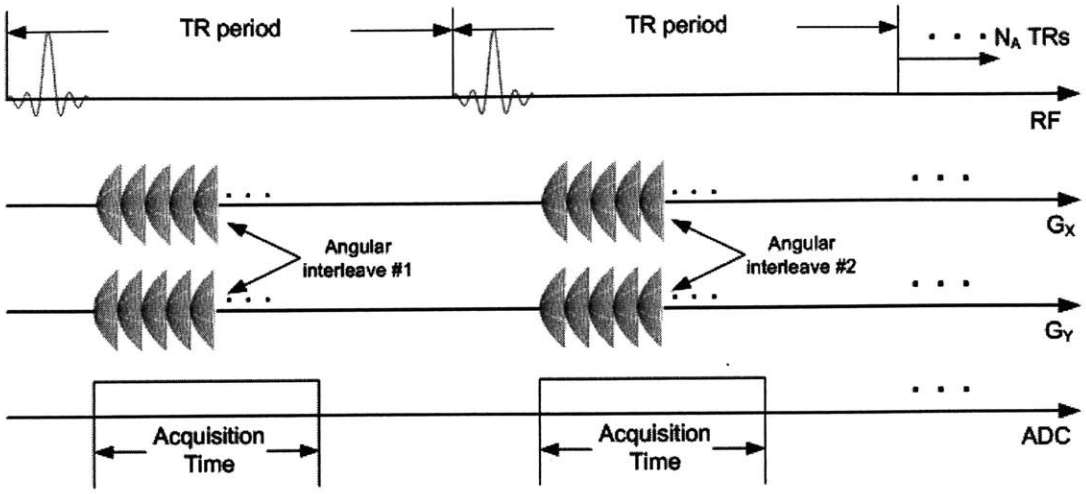

Figure 2-7: Timing diagram showing 2 out of the 4 angular interleaves from Figure 2-6. After the scan is done, the raw data are assembled and reconstructed: The result is spectroscopic data encoded spectrally and spatially.

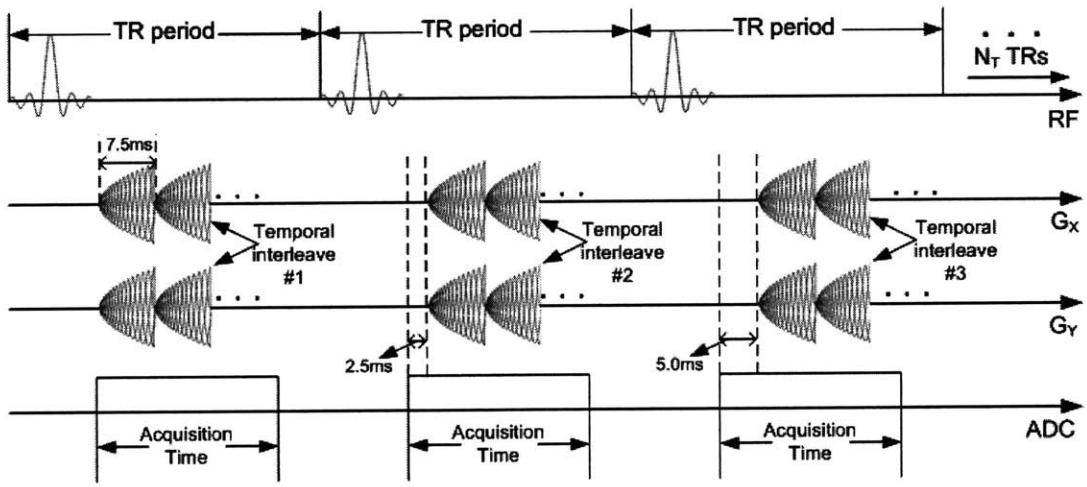

Figure 2-8: Timing diagram showing 3 TR periods, each of which plays 3 (out of N_T) temporal interleaves. The length of one spiral lobe is an integer multiple of the temporal sampling time (uniform temporal sampling is obtained).

The example given above, and shown on Figure 2-8, produces (a desired) uniform sampling along the k_f axis – in this case, every (k_x, k_y) point is temporally spaced $2.5ms$ apart. The reason for this is that the length of the spiral lobe is an integer multiple

of the temporal sampling time. The integer number N_T, obtained from dividing the length of the spiral lobe and the temporal sampling time, gives the number of TR periods used in the scan.

Temporal interleaves (as was the case for angular interleaves) alone are capable of providing a spectroscopic set of data with the constraint that the length of the spiral lobe is an integer multiple of $2.5ms$. If that is not the case, one will obtain (undesired) non-uniformly sampled k_t axis, as every $N_T - th$ sample won't be $2.5ms$ apart from its previous neighboring sample. This is shown on Figure 2-9.

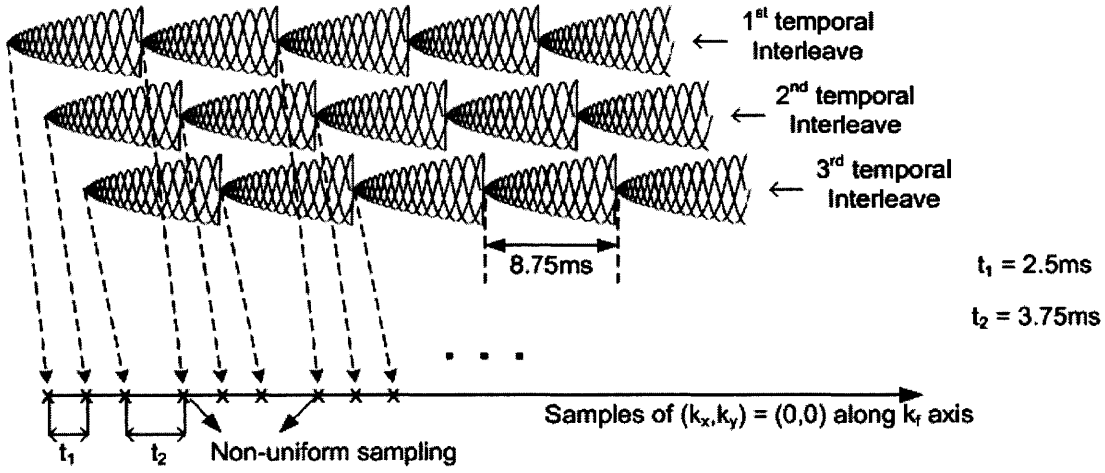

Figure 2-9: The length of one spiral lobe is not an integer multiple of the temporal sampling time and as a consequence a non-uniform temporal sampling is obtained.

Angular and temporal interleaves present two different ways of implementing the Spiral CSI algorithm in the case of the more realistic scenario when the time to traverse the required k-space plane is much longer than the temporal sampling period. The current CSI algorithm is implemented as a combination of both angular and temporal interleaves. As shown, the scan time has been significantly reduced: if a conventional CSI scan encoding 16^3 (k_x, k_y, k_z) locations requires 16^3 excitations, the spiral CSI algorithm (for the same spatial resolution and FOV) will take only 46 excitations (maximum slew 150 T/m/s, maximum amplitude 10mT/m), providing an acceleration factor of 89. Furthermore, the SNR suffered losses only due to the reduction of the acquisition time, but not due to the number of resolved voxels.

2.3.2 Readout part in spiral CSI: Spiral Design

The main objective of this section is not to talk about the explicit spiral design, but rather to comment on the spiral trajectory k-space sampling density and the way it affects the reconstructed data.

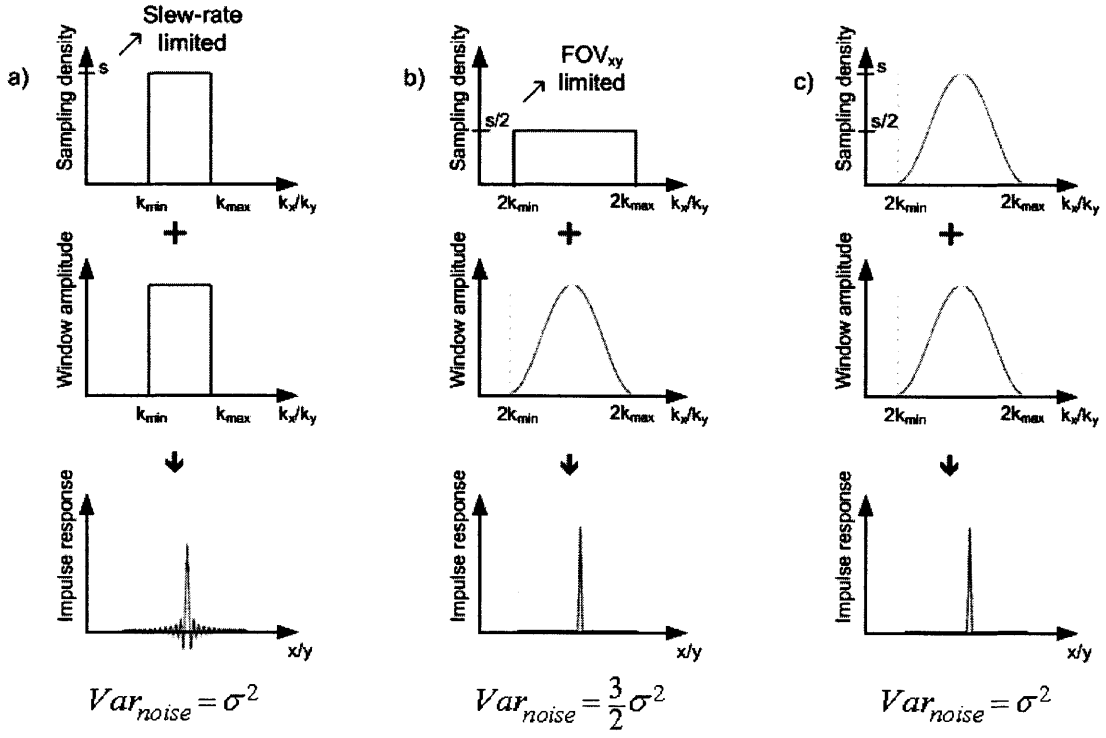

Figure 2-10: a) Constant density k-space sampling, its impulse response, and no windowing used (assuming fixed scan time and voxel size). b) Constant density k-space sampling, its impulse response with Hanning window used. c) Variable density k-space sampling, its impulse response with Hanning window used.

The angular interleaves shown in Figure 2-6 are example of constant-density spiral trajectory. The reason for this name is the fact that k-space positions are sampled uniformly as a function of the k-space radius. If no windowing is applied to the Fourier domain data, the reconstructed data will suffer from significant amount of ringing, which is due to the spatial side lobes of the impulse response (resulting from the circular extent of (k_x,k_y) sampling, and thus a jinc-shaped impulse response). This ringing can significantly contaminate brain spectra, for example due to partially suppressed lipid in subcutaneous fat or large residual water signals from inhomomgenous B_0 regions. This

effect is sometimes called "voxel bleed". The objective now is to reduce the ringing such that the noise level per pixel stays the same, with the constraints that the voxel size and the total imaging time are left unchanged (and therefore the SNR stays the same). Moreover, let's assume that the non-windowed, constant-density k-space sampling scheme (that produces the ringing artifacts) acquires k-space samples between $\pm k_{max}$ and that the noise variance per pixel in the reconstructed data is normalized to σ^2 (see Figure 2-10).

A way to improve the impulse response, i.e. reduce the side lobes, is to pre-window constant density k-space data acquired between $\pm 2k_{max}$ with a Hanning window [28, 29]. For this task, the spiral trajectories used sample k-space twice as sparsely as the original ones (but still satisfying the FOV requirements), so that the constraint on keeping the total imaging time unchanged is fulfilled (Figure 2-10). Moreover, defining voxel size as the area (integral) under the impulse response [29], one can easily observe that the voxel size using this scheme is the same as the voxel size of the original k-space sampling with "voxel bleed" (satisfying the second imposed constrain). In this case, the ringing is substantially diminished, since the Fourier Transform of a Hanning-window-like function has the first sidelobe at about -31.6 dB compared to -13.2 dB for the sinc (see Figure 2-10). The cost however, is increased noise variance, which now is 50% higher than before (i.e. it is $1.5 \cdot \sigma^2$).

Since Hanning-window-like functions reduce side-lobes and uniform density k-space trajectories provide better noise variance, the ultimate solution would be to use variable density k-space sampling schemes followed by Hanning windowing. These variable density spiral trajectories are designed such that their density as a function of k-space radius is proportional to the roll-off of the applied Hanning window as a function the k-space radius [30] (see Figure 2-10). This means that given the shape of the Hanning Window, the k-space sampling should be such that spatial frequencies around DC are sampled much more densely compared to higher spatial frequencies. In other words, the k-space sampling at the edge of the spiral trajectory is completely determined by the spatial FOV requirements. Further, the sampling around the DC point (k-space origin) is completely slew-rate limited: since the objective is to traverse k-space as fast as possible, the gradients are put to their limits when playing this part of the spiral trajectory.

The current spiral CSI algorithm was implemented using a combination of angular and temporal interleaves of variable density (VD) spiral trajectories with the goal large-volume spatial sampling of 400 Hz spectral bandwidth CSI data [31]. For each k_z value, the corresponding $k_x k_y$ plane was traversed using different spirals, as shown on Figure 2-4b: for higher k_z spatial frequencies, high $k_x k_y$ spatial frequencies were not sampled, making the in-plane spirals shorter, and therefore the number of temporal and angular interleaves used for that $k_x k_y$ plane small; for the slices around $z=0$, much denser spiral trajectories were used, leading to more temporal and angular interleaves. The reason for this sampling scheme along the k_z axis is due to the fact that most of the energy of the signal is concentrated around the DC points.

2.3.3 Excitation in spiral CSI: The Spectrally and Spatially selective RF pulses

In order for the readout explained above to give meaningful results, the volume of interest has to be appropriately excited, i.e. limit the spatial extent to the resolved FOV along z, excite all metabolites of interest, and suppress undesired water and lipid signals. In comparison to the excitation problem in structural imaging, excitation in CSI includes "exciting" certain frequency range, in addition to excitation in space. Therefore, to obtain good spectroscopic data one needs to design pulses that are selective in both space and frequency. The first task in this section will be to give concise description of one approach to CSI excitation through spectral-spatial (SPSP) RF pulses [12, 32-34], followed by short discussion on the spin-echo (SE) RF pair used in the spiral CSI acquisition.

Let's leave the spectral selectivity aside for a moment and see how spatially selective RF pulses work. An intuitive way to understand this is given by what is known as the "small tip angle approximation" [35]. If an RF pulse is played out together with a gradient, the spatial region excited corresponds to the Fourier transform of the function obtained from values of the RF pulse at excitation k-space locations defined by the gradient. In other words, the RF pulse will deposit energy onto the k-space at positions determined by the gradient, and the Fourier Transform of this function will produce the

excited area/volume of interest [35]. For example, if the G_z channel and the RF channel take the shape of a trapezoid and a sinc function respectively, the resulted excited region will be a rectangular function along the z spatial dimension (see Figure 2-11)

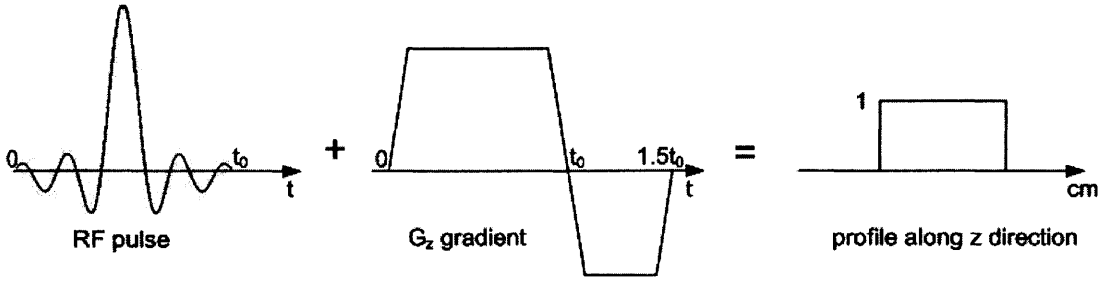

Figure 2-11: Spatially selective RF pulses. Trapezoid gradient is played on the z gradient channel and a Sinc function is played on the RF channel. The resultant excited profile is a rectangular function along the z axis.

A more complicated example would involve 2D excitation where playing appropriate waveforms *on the RF and two gradients channels* would produce 2D spatial selection. Thus, if the RF pulse deposits energy on k-space locations in the $k_x k_y$ plane, the 2D region that gets excited will be the Fourier Transform of the 2D function obtained when values of the RF pulse are put onto the correct (k_x, k_y) locations. Although the 2D spatial excitation is not within the scope of this thesis, it is worth mentioning its basic idea, as designing SPSP pulses involves nothing more but replacing one of the two spatial axes with a temporal axis (with a bit of adjustments discussed later in this section).

In summary, RF pulses are designed to deposit energy along k_f, and let's say, k_z axes. Determining the k_z locations where the RF energy is to be deposited is done with the G_z gradient. In order to deposit energy along the k_f axis, and since phase accrual in chemical shift can be thought of as due to a constant "gradient", G_f, one would suggest that playing out the RF pulse repeatedly in time would be able to excite a particular profile in (z, f). Before giving a bit more elaborate explanation of what was just said, it is worth mentioning that [12, 32-34] have detailed description of the design and implementation of the SPSP RF pulses. Further the next couple of paragraphs summarize what can be found in Section 5.4 of [5].

Imagine that the objective is to select signals within certain frequency range that belong only to a slice (with defined thickness) along z direction. The slice selection can be easily done with a sinc function, $S_{space}(t)$ (from now on referred also as the sub-pulse), and trapezoid gradient played on the RF and G_z channel respectively. From the Fourier Transform properties, selecting certain frequency range corresponds to playing out a sinc-like function, $S_{spec}(t)$ as time passes by. Therefore, the shape of the SPSP RF pulse will be a combination of $S_{space}(t)$ and $S_{spec}(t)$. Since the spatially-selective gradient has to be played out repeatedly in time in order to fill in the $k_z k_f$ plane with RF energy appropriately, the final shape of the SPSP RF pulse will consist of multiple repetitions (in time) of $S_{space}(t)$ modulated by the shape of $S_{spec}(t)$ (the envelope of the final pulse).

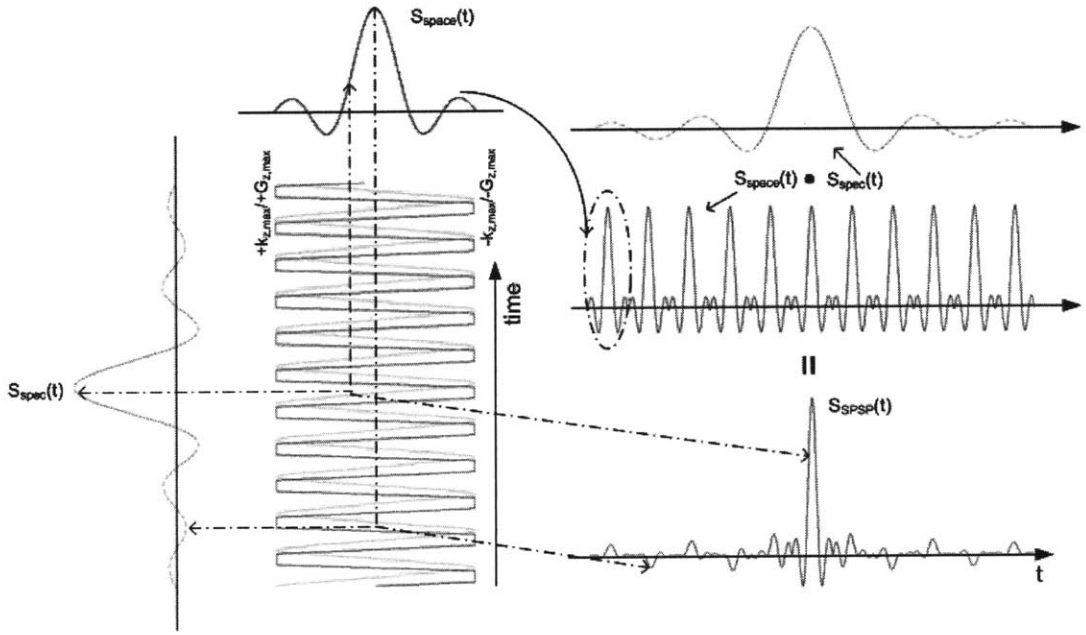

Figure 2-12: Generating a spectral-spatial RF pulse. Its shape is determined by multiple repetitions (in time) of the spatially-selective RF pulse, modulated by the shape of the function responsible for the spectral selection.

During the multiple repetitions of the spatial sub-pulses, periodic, trapezoid-like G_z gradient with period T is being played. The period T depends on the duration of the overall SPSP pulse, T_{SPSP} (i.e. the length of $S_{spec}(t)$) and on the desired slice thickness. Firstly, for a given slice thickness, one finds the smallest possible value, $T_{\min}$, thereby

using the full slew-rate and maximum gradient amplitude available. Secondly, the value of $N = \lfloor T_{SPSP}/T_{\min} \rfloor$ is obtained, which would determine how much one needs to increase $T_{\min}$ in order to get the final value of T, such that T_{SPSP}/T is an integer.

Figure 2-12 represents nice pictorial description of how the shape of the SPSP RF shape is being generated. It shows periodic trapezoidal gradient with period T and the shapes of the sub-pulse ($S_{space}(t)$) on the top, and the envelope ($S_{spec}(t)$) on the left. At any time, the value of the final shape of the pulse is given by $S(t) = C \cdot S_{spec}(t) \cdot S_{space}(t)$, such that $S_{space}(t)$ is evaluated along $k_z(t)$ (depicted by the dotted line), $S_{spec}(t)$ is evaluated along $k_f(t)$ and C is a constant factor. The excitation region will have a shape of a 2D box selecting certain z location and certain frequency range.

For the purposes of implementing the spiral CSI algorithm, a spin-echo Spectral-Spatial RF pulses were used. The shape of *the real part* of 90 and 180 degrees flip angle pulse and the shape of the corresponding G_z gradients is shown on Figure 2-13.

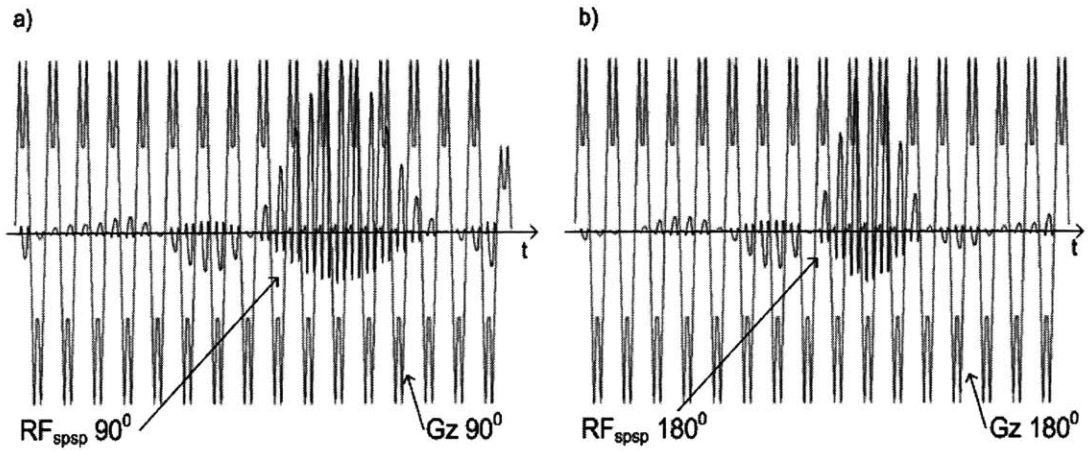

Figure 2-13: Shapes of the real part of the Spin-Echo Spectral-Spatial RF pulses together with the appropriate gradients; a) the 90^0 flip RF pulse; b) the 180^0 flip RF pulse.

Note that the G_z gradient lobe is not a simple trapezoid, i.e. it has a dip on the part where a regular trapezoid shape should be flat. Without going into details, since it is not within the scope of this thesis, the reason for this shape is to reduce the B_1 peak power since "passing through" the $k_z = 0$ is slower (Figure 2-13), compared to the case of the regular trapezoid gradients (Figure 2-11). In other words, keeping the area under the

gradient lobe unchanged, the trapezoid shape in Figure 2-13 allows the RF channel to deposit less energy around $k_z = 0$ to satisfy peak-B1 constraints compared to the case of Figure 2-11, since more RF energy is needed for the same task in order to "keep up" with the faster changing area under the regular trapezoidal gradient.

2.3.4 Excitation in spiral CSI: The Adiabatic RF pulse

The last item to be discussed in the design part of the thesis is the adiabatic RF pulse. A common use of adiabatic pulses is for inversion (180° flip angle of Mz) that produces constant flipping of the M_Z magnetization for wide range of RF amplitudes [36-39]. This is a useful property in the presence of inhomogeneous B1 since the designer does not need to fine tune the amplitude of the inversion pulse in order to obtain a perfect 180° magnetization flip (which can be a difficult task depending on B1 inhomogeneities) – as long as the adiabatic pulse amplitude is within relatively wide range, the magnetization vector is guaranteed to be appropriately flipped.

Adiabatic pulses fall into the general category of phase-modulated pulses, i.e. they are accompanied by a phase function that is not a constant (Figure 2-14). This implies that the effective flip angle of the adiabatic pulse is *not* given by the area under the pulse shape.

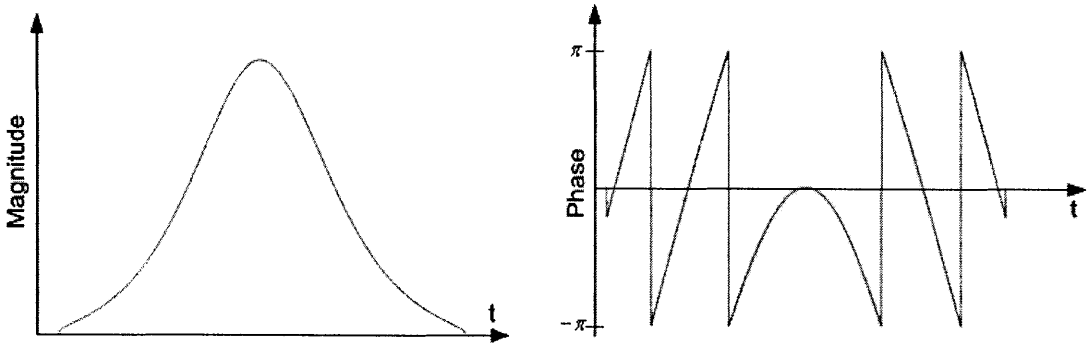

Figure 2-14: Magnitude and phase plots of the inversion adiabatic pulse

In the spiral CSI acquisition, an adiabatic inversion pulse was used for the purposes of nulling one component of T1 in the signal coming from lipids. Due to its molecular structure, the lipid signal shows several separate peaks on the frequency axis, two of

which are in the 0.9-1.3 ppm range, and one around 2.3ppm, between the NAA and Cho resonances. Each of these peaks has different T1 and T2 constants, and therefore it is impossible to get rid of the entire lipid signal simultaneously and at once by a single inversion. In order to improve lipid suppression, the adiabatic pulse is to be tuned such that most of the signal coming from the two lipid peaks around the NAA are nulled.

There are two aspects in the process of fine tuning the adiabatic pulse. First, one needs to make sure that the magnitude of the pulse is within the range of amplitudes that guarantees 180° flips. The second involves finding the correct time of inversion (TI), i.e. the time at which the M_z component of the lipid during its process of relaxation obeyed by the T1 constant), passes through zero. It is at this time that the excitation Spectral-Spatial 90° RF pulse is to be played, ideally resulting in no fat signal excitation (since at this time, $M_z = 0$).

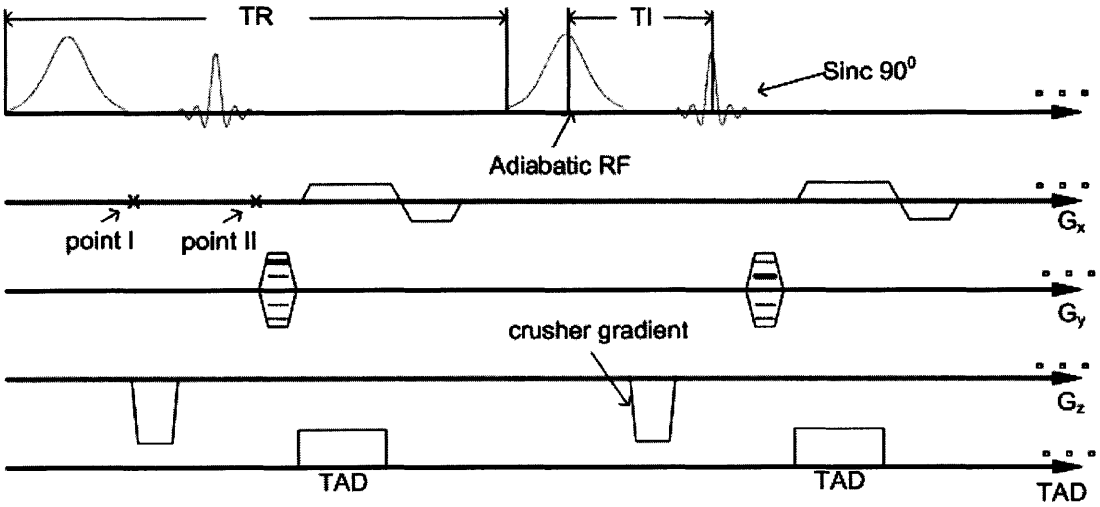

Figure 2-15: Timing diagram of the sequence used to find the right amplitude of the adiabatic inversion pulse.

Determining the correct amplitude of the adiabatic pulse was done by scanning a water phantom with a sequence shown on Figure 2-15 which is a regular 2DFT sequence with the adiabatic pulse added at the very start. Let's follow the magnitude of the longitudinal and traverse magnetization at point *I*. Depending on the amplitude of the adiabatic pulse, A_{AP}, the magnitude of the longitudinal magnetization will be different at point *I*. This magnetization will then be nutated to the transverse plane and the signal for

a specific k_y line will be acquired. Reconstructing the data after the scan is finished and measuring the mean value of an area within the phantom, denoted as A_{TR}, will give us quantitative measure of the how much the adiabatic pulse has tipped the longitudinal M_z magnetization from its initial position. Further, we have repeated this scan, each time changing the value of A_{AP}. Starting with low amplitude, the value of A_{TR} would initially be large (M_z is almost perfectly aligned with B_0) but it will always be decreasing as A_{AP} increases. Eventually, A_{TR} is expected to remain constant despite of further A_{AP} increase, alluding to the fact that at that point A_{AP} is within the amplitude range where we are (theoretically) guaranteed an 180^0.

Figure 2-16 shows the *amplitude* of A_{TR} as a function A_{AP}. This plot is consistent to what was said in the last paragraph. The value used for the appropriate scaling of the adiabatic pulse was chosen somewhere in the middle of the flat region I Figure 2-16, which corresponded to ~150V peak RF voltage.

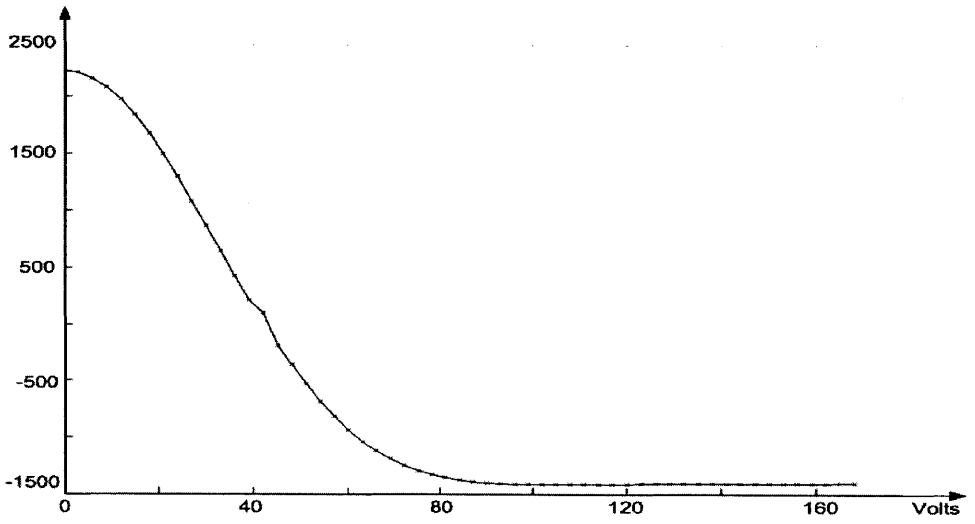

Figure 2-16: Testing the magnitude of the adiabatic pulse. Vertical axis represents the mean value of an area within the reconstructed phantom image, which gives direct measure of the longitudinal magnetization, M_Z. The horizontal axis shows the peak RF voltage applied to the adiabatic pulse. It can be seen that any voltage above 80V guarantees 180° flip of the longitudinal magnetization.

After determining the correct amplitude of the adiabatic pulse, the final thing left to be done is to determine the correct value of the time of inversion (TI). As shown in Figure 2-15, the TI time is measured from the peak of the adiabatic pulse to the peak of

the excitation pulse. Having in mind the relatively short T_1 relaxation times of the lipids ($T_{1L} \simeq 245ms$) the value of TI was tuned to minimize the lipid signal at the echo time of 288ms [40], and it was experimentally found to be around $170ms$. Fine-tuning was done by recording FIDs from non-spatially selective spectroscopic scans (only thin slice along the z axis was excited) each of which played with different values of TI. Total of 20 experimental scans were performed with $TE = 288ms$, and the values of TI ranging from $166-188ms$. Acquiring spectra with no spatial encoding, and recording the values of these spectra at 0.9, 1.3 and 2.3 ppm, gave quantitative measure of the amount of signal present from each lipid. Figure 2-17 puts these points on one plot. From this, it can be seen that the best that we can hope for is completely nulling the lipid component at 1.3 ppm, which happen for $TI = 172ms$.

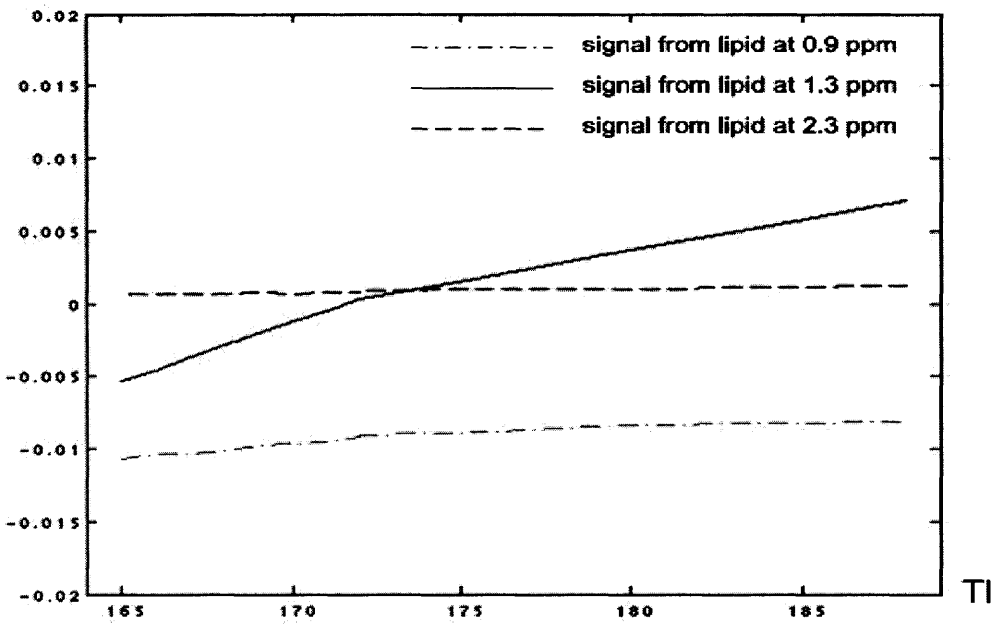

Figure 2-17: Testing the TI time. The blue, plotting the peak of the lipid at 1.3ppm as a function of the inversion time, clearly crosses zeros for TI = 172ms, corresponding to nulling this particular lipid component. Two subjects were used to obtained the data: the first one for scans with TI < 174ms, the other for scans with TI > 172. After the scans were done, the data was combined to obtain the above plot.

With this, I conclude the discussion on the theory and design of the spiral CSI algorithm. What was presented gave an overview of the different parameters used in the process of implementing the spiral CSI algorithm and set the basis for the discussion of the next task in this project: reconstruction of the spectroscopic data. This will be topic of the next chapter.

3 Spiral CSI Multi Coil Reconstruction

Here, I discuss the reconstruction of CSI data obtained by spiral CSI sampling at 1.5T. Currently the reconstruction process is done offline, using programs written in MATLAB and C. The Siemens MR platform used to acquire the data has its own reconstruction environment (called **I**mage **C**alculation **E**nvironment, or ICE), and at the moment of writing this thesis, we have initiated the transfer of reconstruction code onto the ICE platform.

The data obtained from the scanner are Fourier-domain data, i.e. raw data files created directly from the analog-to-digital converter (ADC). As mentioned in the previous chapter, the Spiral CSI algorithm used FOV_{xy}/FOV_z = 24cm/12cm, $N_x/N_y/N_z/N_f$ = 64/64/32/256 points, slice thickness of 0.375cm, and TI/TR/TE = 288ms/2s/288ms. The duration of readout was 400ms (the time that the ADC was turned on during one TR). Given that the sampling rate used in the Spiral CSI scans was $4\mu s$, 100,000 complex floating points per TR and per receiver coil were dumped into the raw data file. Having 228 TRs in one 3D volumetric Spiral CSI scan, and for the case when 23 channel coil array was used for receiving the signal, the size of the raw data file exceeded 4GB. Although the rate at which data was being dumped into the raw file was high (about 46MB/s), the fast Raid Disk used (on a Siemens VB11D® software package) for data storage during collection proved reliable.

The two files per scan were obtained from the scanner: `meas.out` holding the raw data and `meas.asc` holding the values of the parameters used in the scan. Each scanning session involved 3 different scans:

- *Reference CSI*: 4 minutes ($TR = 1s$) on-resonance-frequency reference 3D volumetric scan used for phasing the metabolite data for the purpose of proper multi coil reconstruction (details later in the chapter);
- *Metabolite CSI*: Two (for the purposes of better SNR) 8 minutes ($TR = 2s$) 3D volumetric Spiral CSI scans showing the metabolites spectra.
- *RF Coil Profile*: Regular (not spectroscopic) 3D scan obtaining the profiles of the coil array used for reading out the signal from the same 3D volume excited by the Spiral CSI scan (used for the multi coil reconstruction).

These ~17GB worth of data were transferred to a portable Hard Drive and then fed to the reconstruction programs. On the highest level, these are the steps involved in the reconstruction process:

- Reconstruct the reference and spectroscopic 3D volumetric data sets for each coil channel, separately.
- Use the reconstructed reference set to perform appropriate phasing of the reconstructed metabolite data set (this is again done for every coil separately).
- Use the coil profiles to appropriately weight the individual coil data in order to combine them, and generate a single 3D volumetric spectroscopic data set.

Before going into detailed discussion of the above three steps, it is instructive to point out some important verification tests, which can be used to improve results. Further, this chapter will also include the improvement of a prior implementation of the gridding algorithm, using the fact that samples along the k_t axis are sampled uniformly. Towards the end of this chapter, the result's section will verify that the reconstructed data obtained verify the theoretical statement that using multi channel receive coil array in Spiral CSI improves the SNR, compared with the single coil case.

3.1 Calibration Scans

This section considers two issues, important for insuring that the results obtained from the reconstruction algorithm do not suffer from undesired artifacts. The first issue addressed is checking that the selected on-resonance frequency stays unchanged

throughout the scans. The second issue involves checking whether there is any spatial frequency drift (in the $k_x k_y$ plane) as the spiral lobes are played out.

3.1.1 On-resonance frequency drifts

Once the central frequency used in a particular scan is manually selected before the scan can takes place, it is important for the selected frequency to stay unchanged throughout the whole scan. The reason is obvious: frequency drifts throughout the scan will cause undesirable artifacts on the final spectra, in a way that the metabolite peaks will be smeared out, causing the SNR of the spectra to be significantly lower. This frequency drift might be a consequence from heating of the gradients and subsequent drift of shim terms, mainly if the gradients are used at the limit of their maximum amplitude and slew rate specifications. This is the reason why the spiral trajectories used in the Spiral CSI algorithm were not designed at the gradient's limit specifications.

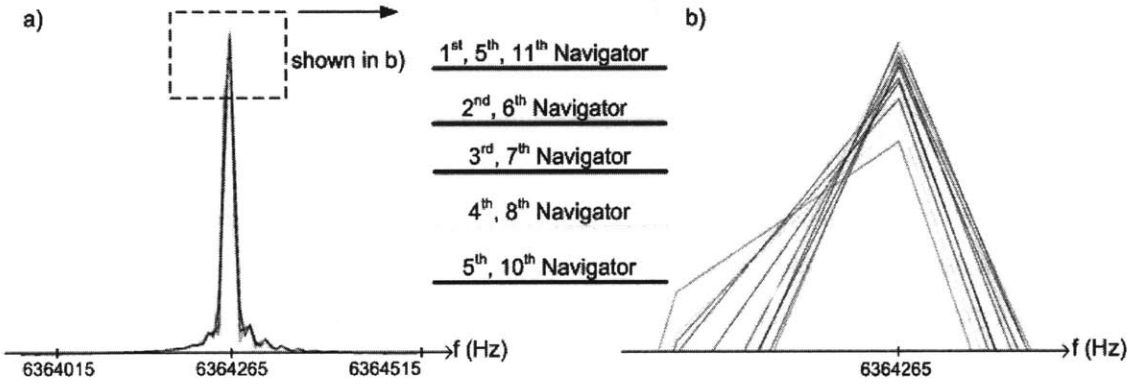

Figure 3-1: Checking for on-resonance frequency drifts: a) The 11 spectra from the frequency navigators of a reference (4 minute) scan are over plotted one on top of another. Different color correspond to spectrum from a different navigator; b) The box selected in a) zoomed in: this verifies that the frequency doesn't drift throughout the scan.

Checking for on-resonance frequency drifts was done by reading the FID signal every 20th TR period. In other words, the ADC stayed turned on, but the spirals on G_x and G_y channels were not played every 20th TR. This modification resulted in non-significant extension of the overall time of the scan, which was terribly bad in terms of time constrains: originally there were 228 TR periods, and after putting these frequency navigators every 20th TR, the scan had 239 TR periods, resulting in 22 seconds increase of overall scan time.

After acquiring these frequency navigators, they were appropriately extracted from the rest of the true CSI data, and 11 FIDs per coil used were obtained. Fourier transforming these FIDs and over plotting them on the same graph showed that the Spiral CSI scans did not suffer from measurable frequency drifts. Figure 3-1 verifies this pictorially using the navigators from the 4 minute reference scan, where one would expect that the spectra would show one frequency peak corresponding to the resonance frequency of the water molecules.

3.1.2 Spatial Frequency drifts

Besides on-resonance frequency drifts, spatial frequency drifts can also cause significant amount of artifacts in the reconstructed spectroscopic data. Spatial frequency drifts are type of drifts where the gradients do not track the specified k-space trajectory designed by the programmer. For example, if the designer asked the gradients to spiral out the k-space in time t_o, and spiral back in time t_i, one would say that the scan suffers from spatial frequency drifts if the reconstructed data at time $t_o + t_i$ show that the sampled data are not obtained at (kx,ky)-space origin (theoretically we should be exactly on the (kx,ky)-space origin) [41].

Having in mind that within one acquisition time (400ms), particular spiral lobe is repeated multiple times, one way to check for spatial frequency drifts is to see whether the peak of the $k_x k_y$ in-plane raw data (for a particular time instance) in between any two consecutive spiral lobes is at the k-space origin. Looking for a peak in between spiral lobes in Spiral CSI makes sense due to couple of reasons: 1. each spiral lobe, by design, rewinds itself to the k-space origin, so that at the next repetition the same k-space trajectory is traversed; 2. peak at k-space origin is logical since that is the DC point, i.e. the area of the object being scanned. Having said this, if the gradients were "going off track", the peak of the in-plane raw data would not have been at the k-space origin.

Acquiring the data for this testing was done on a cylindrical water phantom using a version of the Spiral SCI algorithm that only excites one slice and included two angular and six temporal interleaves. Since, by definition, the signal around TE is the strongest, its value was tuned such that the effective spin echo took place in between two spiral

lobes, i.e. when supposedly $(k_x, k_y) = (0,0)$. The objective of the experiment then was to see whether the peak of the raw data drifted more from the k-space origin as the number of spiral lobes played before the effective spin echo increased.

Figure 3-2 shows the raw data obtained from the first two angular interleaves of the spiral lobe right before the spin echo, plotted as a function of the designed k-space trajectories. Different values of TE were chosen such that exactly 2, 6 10 and 14 spiral lobes were played before the effective spin echo. Several things can be observed:

- There are indeed small measured offsets of the raw data peak values from the k-space origin. Given this fact, a sanity check would be to verify that the peak locations from the 2 angular interleaves (0° and 180°) are roughly a complex conjugate pair, i.e. if the peak of the one is in the first quadrant, the peak of the second one would have to be in the third quadrant. The numbers in Table 1 suggest that this is indeed the case.
- Although for earlier TE the drift is minimal, increasing the number of spiral lobes before the effective spin echo doesn't seem to linearly increase the drift from the k-space origin. As a matter of fact, having the TE after the 14th spiral lobe produces smaller spatial frequency deviations from $(k_x, k_y) = (0,0)$, compared to the case when the TE is after the 6th and 10th spiral lobe.

Table 1: Peak signal values and their (kx,ky)-space location for different values of TE.

Spin-Echo after	0° angular interleaf			180° angular interleaf		
	Max	k_x (cm^{-1})	k_y (cm^{-1})	Max	k_x (cm^{-1})	k_y (cm^{-1})
2 lobes	0.0403	-0.0807	-0.6898	0.0406	0.0156	0.4990
6 lobes	0.0255	-0.6570	-1.7780	0.0257	0.5761	1.5895
10 lobes	0.0163	-0.6570	-1.7780	0.0161	0.5761	1.5895
14 lobes	0.0101	-0.4579	-1.4176	0.0102	0.4744	1.1906

The last point implies that the spatial frequency drift is not a linear function of the duration of the gradients. These small drifts could happen due to eddy-currents or incomplete modeling of the k-space trajectories based on the gradient waveforms.

Further if one were to correct for these drifts, the G_x and G_y correcting gradients would have had tiny amplitude and one might come across gradients quantization issues. For example, in the case when the TE is at the start of the 14th spiral lobe the k-space needed to be corrected for is given as (the numerical values seen in Table 1)

$$\begin{aligned} \Delta k_x &= \Delta k_{x\_ang180} - \Delta k_{x\_ang0} = 0.9323 \\ \Delta k_y &= \Delta k_{y\_ang180} - \Delta k_{y\_ang0} = 2.6082 \end{aligned} \tag{3.9}$$

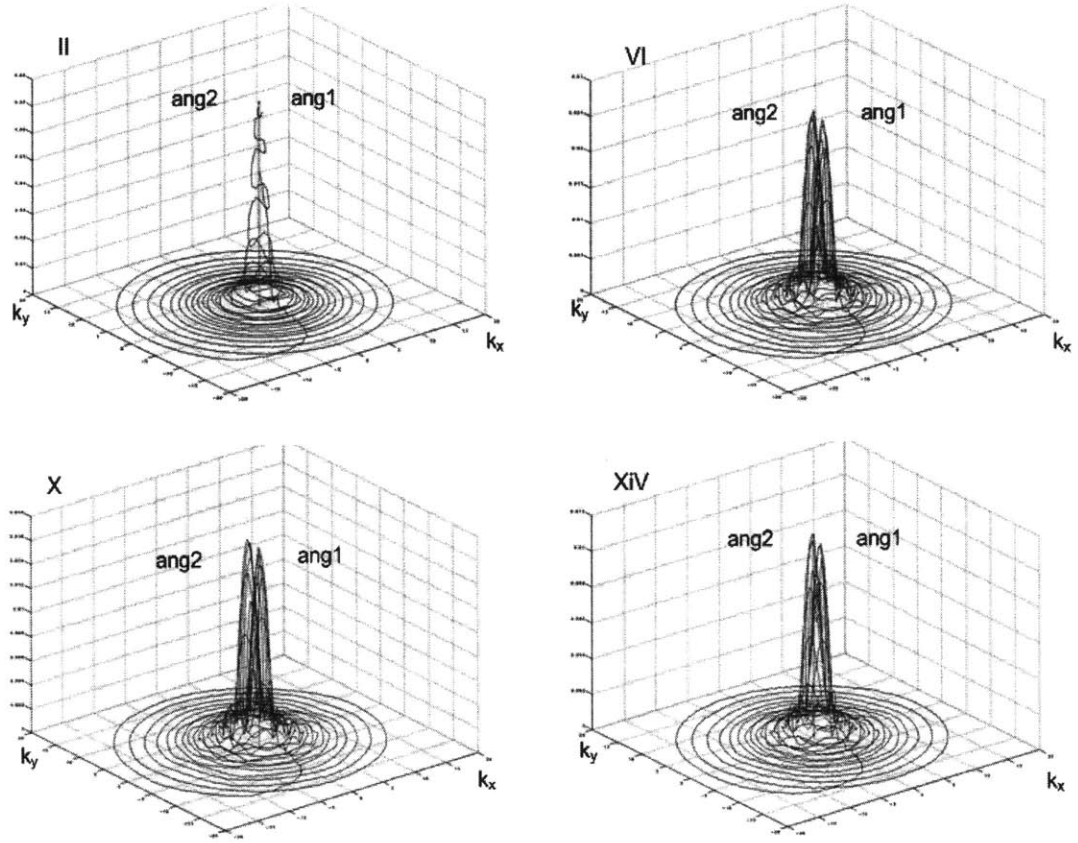

Figure 3-2: In plane raw data for two angular interleaves of the spiral lobe just before the effective spin echo. In the graphs above, TE was tuned to happen right after: a) 2 spiral lobes; b) 6 spiral lobes; c) 10 spiral lobes; d) 14 spiral lobes;

Given these values for Δk_x and Δk_y, the amplitude of $10\mu s$ long G_x and G_y needed to be played *after each spiral lobe* in order to do the correction, is given as follows:

$$G_{x\_corr} = \frac{1}{14} \cdot \frac{\Delta k_x}{(\gamma/2\pi) \cdot t_{x\_corr}} = \frac{1}{14} \cdot \frac{0.9323 cm^{-1}}{42.58 \frac{MHz}{T} \cdot 0.01 ms} = \boxed{1.564 \cdot 10^{-3} \frac{mT}{m}}$$

$$G_{y\_corr} = \frac{1}{14} \cdot \frac{\Delta k_y}{(\gamma/2\pi) \cdot t_{y\_corr}} = \frac{1}{14} \cdot \frac{2.6082 cm^{-1}}{42.58 \frac{MHz}{T} \cdot 0.01 ms} = \boxed{4.375 \cdot 10^{-3} \frac{mT}{m}} \quad (3.10)$$

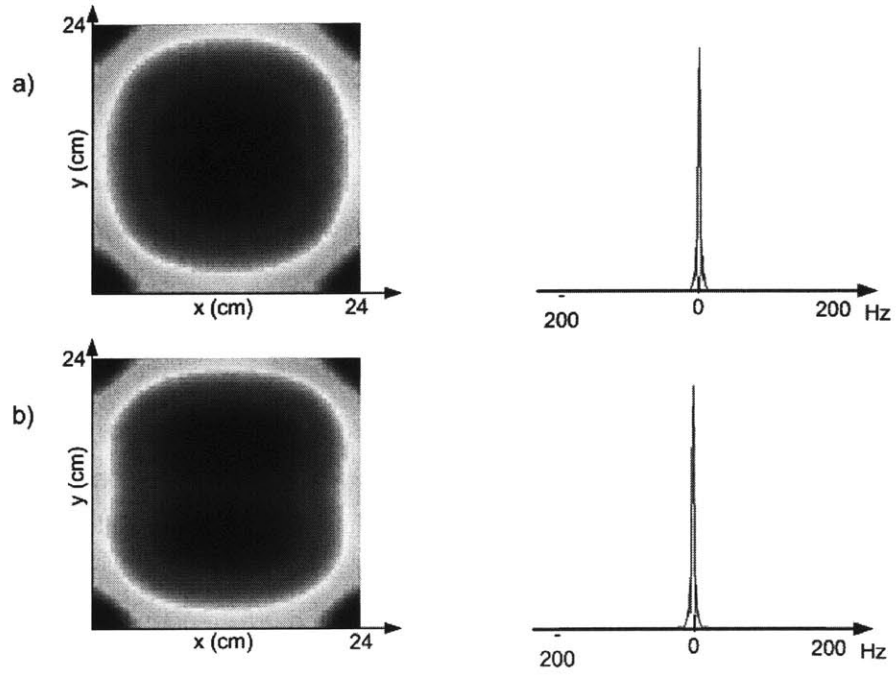

Figure 3-3: Determining the effect of the spatial frequency drifts recorded by feeding the reconstruction routine with synthesized raw data of a large-FOV object; a) Reconstruction results using the original k-space trajectory. b) Reconstruction results using modified k-space trajectory that reflects the numerical values of the spatial frequency drifts from Table 1. The dip that can be seen in the middle of the image is about 1.2% lower than the maximum value.

In order to experimentally show that these small spatial frequency drifts do have some (albeit small) effects on the reconstructed data, we did simulation of a large-FOV object reconstruction with and without these offset. Figure 3-3a shows reconstruction results of a synthesized large-FOV object using the original k-space trajectories. Figure 3-3b, on the other hand, shows reconstruction results using k-space trajectories that have been modified to incorporate the spatial frequency drifts presented in Table 1. Looking at these figures, one can easily observe that although the spectra in the two cases look essentially identical, there is indeed a slight cosine-like modulation in the

(x, y) plane, which is consistent with the numerical values in Table 1). Although this artifact is has a relatively small impact on the reconstructed data, the results shown in Figure 3-3 suggest it is desirable to incorporate corrections of these artifacts.. There are two solutions to this problem: 1. Supply small correction gradients at the end of each spiral lobe during data acquisition and 2. Modify the k-space trajectory to account for these drifts during gridding reconstruction. Both of these will be explored in future work.

With this, the section discussing the calibration scans can be put to an end. Next, the reconstruction will be addressed.

3.2 Single Coil Reconstruction

Although the spectroscopic data were always acquired with multiple coils, the same reconstruction method was applied to every coil individually before the coils were combined. This section will exploit the single coil reconstruction and verify its correctness by observing the results from one of the coils used.

The initial task, even before the reconstruction took place, was to separate the raw data from all the coils into different files, each holding data from only one coil. The reconstruction program (written in C) used two header files as an input, in addition to the file holding the raw data for a particular coil. These two header files were known as the `kfile` and the `parfile`. The `kfile` held the k-space trajectories matching the locations traversed by the gradients during the scan. The `parfile` held values for scan parameters such as FOV, resolution, apodization, etc. At the end of the reconstruction, data were 4-dimensional, complex sets of 64x64x32x256 voxels encoded in (x, y, z, f). This 4D space consisted of samples placed on a Cartesian grid, since the reconstruction algorithm performed gridding on the non-uniformly sampled Fourier domain (k_x, k_y) data (discussed in the next section).

For every value of z, the 3D set of data was represented in 2 different files with extensions `.ic.t` and `.rc.t` which were holding 64x64x256 complex valued matrices of the object domain (encoded in (x, y, f)) and Fourier domain (encoded in (k_x, k_y, k_f)) gridded data, respectively. Having 32 slices in a scan, a total of 64 of these files were generated.

I will start this section by brief and concise description of how gridding was used to reconstruct the data in the current version of the reconstructed algorithm. This discussion will lead to the discussion of how one could make the implementation of the gridding more efficient for the sampling patterns used in the current version of the Spiral CSI algorithm. We will continue with a discussion of the process of appropriately phasing the object domain data (critical for multi-coil reconstruction), and conclude this part of the thesis by showing spectra for several values of (x, y, z) from one coil.

3.2.1 The gridding algorithm used in Spiral CSI

Gridding is known to be one of the most efficient and practical ways to reconstruct non-uniformly sampled Fourier domain data [42-44]. At its core, gridding is simply convolving the non-uniformly spaced samples by a small kernel and sampling the output onto a uniform grid. After this, fast Fourier transform (FFT) can be used to quickly generate the object domain data. Let's say, we have samples that are non-uniformly sampled in a 3D space, forming some function $F(k_x, k_y, k_z)$. Ideally, convolving $F(k_x, k_y, k_z)$ with a kernel function $H(k_x, k_y, k_z)$ that is an infinite sinc, re-sampling the result onto a Cartesian grid and doing FFT, would produce object domain function $f(x, y, z)$ that would be exactly the same as the function obtained by directly doing DFT on $F(k_x, k_y, k_z)$. However, infinite sinc functions as kernels are impractical, and the computation time for regular DFT is long. Therefore, small kernel functions are used in practice, the most common being simple triangular, Bessel function of first order, or cone-like functions [45, 46].

The gridding algorithm used in the spiral CSI reconstruction treated the 4D space of (k_x, k_y, k_z, k_f) points as being entirely non-uniformly sampled (although that is certainly not the case, since k_f and k_z points are uniformly sampled – this issue will be address later). After the raw data are fed into the reconstruction program, the first task is to re-order them. Knowing the number of angular and temporal interleaves (and therefore the number of TRs) of a particular k_z location, the raw data from these TR periods is appropriately put into the (k_x, k_y, k_z) matrix. For example, if for the 16th slice the number of temporal and angular interleaves was 6 and 2, respectively, then the raw data of the

first 2 TRs (i.e. the 2 angular interleaves of the first temporal interleave) will fill in the k-space positions for all values of k_x and k_y and every 6th value of along k_f, i.e. the $(k_x, k_y, k_f/6)$ locations. Similarly the 3rd and the 4th TR will contribute to the $(k_x, k_y, (k_f/6)+1)$ positions and so forth. This is repeated for all 32 slices to finally create the (k_x, k_y, k_z, k_f) matrix to be gridded.

Before gridding the data, there is some preprocessing needs to be done on the 4D data along k_x and k_y, the directions where the spirals are played. Due to the fact that *variable density* spiral trajectories were played, (k_x, k_y) region that is around the DC point is sampled much more compared to the rest of the in-plane k-space. Interpolating this region with the kernel function will make samples on the rectangular grid closer to DC to have numerical values that are higher that they suppose to be. Thus, the raw data along k_x and k_y (for a certain slice) is to be multiplied with a compensating density function that will give less weight to samples around DC and more weight on samples at higher $k_x k_y$ frequencies. Having done this, the gridding can start. After it is done, the uniformly spaced data is multiplied by the inverse of the Fourier transform of the kernel function in order to account for the apodization effect, a consequence of the Fourier transform properties (convolving k-space data with the cone-like function is multiplication of the object domain data with the Fourier Transform of the cone-like function). Nice detailed description of what was just said is given in [46].

Reconstruction of 3D spectroscopic data from one coil took about three minutes on dual-processor 2GB RAM/2GHz Linux box. Part of the reason for this reconstruction time is due to the fact that the current version of the gridding algorithm naively considered the (kx,ky,kz) dimensions of interest to be non-uniformly sampled. This, off course, is never going to be true along the k_f direction as the ADC on the system is a uniform sampler. How one would go about and speed up the gridding algorithm taking advantage of these facts, is to be discussed next.

3.2.2 Improvement of the current gridding algorithm

Given the linearity of the Fourier Transform and the fact that samples along k_f are uniformly spaced, the gridding algorithm currently used can be improved by doing FFT along the k_f direction (with some appropriate adjustments) and excluding this direction in the gridding process. In order to avoid cumbersomeness, let's assume encoding in the (k_x, k_y, k_f) space only. The goal of this section is then to prove (theoretically and experimentally) that reconstructed data obtained from 3D gridding and from applying the proposed improved method are identical.

The theory behind this idea is a straightforward consequence of the Fourier transform properties, i.e. from the fact that shifts in time (object) domain corresponds to phase offsets in the temporal (spatial) frequency domain. Having this in mind, the proposed improvement in the case of spiral CSI is obtained is a four-step process discussed next.

Firstly, samples from all the angular and temporal interleaves have to be appropriately rearranged in 3-dimensional (k_x, k_y, k_f) vectors such that for each value of (k_x, k_y) we have a FID signal. Note that this will not be the case if one is to simply take the raw data from each TR period sequentially. For example, consider the samples of the FID of the DC point $(k_x = 0, k_y = 0)$ for the case when we have 3 temporal and 2 angular interleave: the first time sample is represented by the first acquired sample of the 1st TR period, but the second time sample is represented by the sample acquired $2.5ms$ into the 3rd TR period! For clarification re-vist Section 2.3.1 and look at Figure 3-4.

Secondly, all the samples in the vector (FID) for a particular $(k_{x,c}, k_{y,c})$ location have to be phase corrected using a constant phase term of the form $\exp(-i \cdot \Delta t \cdot s_c)$. Here, $\Delta t = 4\mu s$ (the sampling time of the ADC), and s_c denotes the sample number such that t_0 (t_{DC}, respectively) is the time at which the sample $(k_{x,c}, k_{y,c})$ ($(k_x = 0, k_y = 0)$, respectively) is acquired.

Thirdly, we perform N_{SP} N_f-long FFTs along the k_f direction. Here, N_{SP} is the number of the spiral points used to traverse the desired k-space, i.e. the number of

samples in one spiral lobe multiplied by the number of angular interleaves (re-visit Section 2.3.1 for clarification). N_f is the number of time samples for a particular (k_x, k_y) point. Having a temporal sampling of $2.5ms$ and an acquisition time of $400ms$, N_f is at most $400ms/2.5ms = 160$ samples.

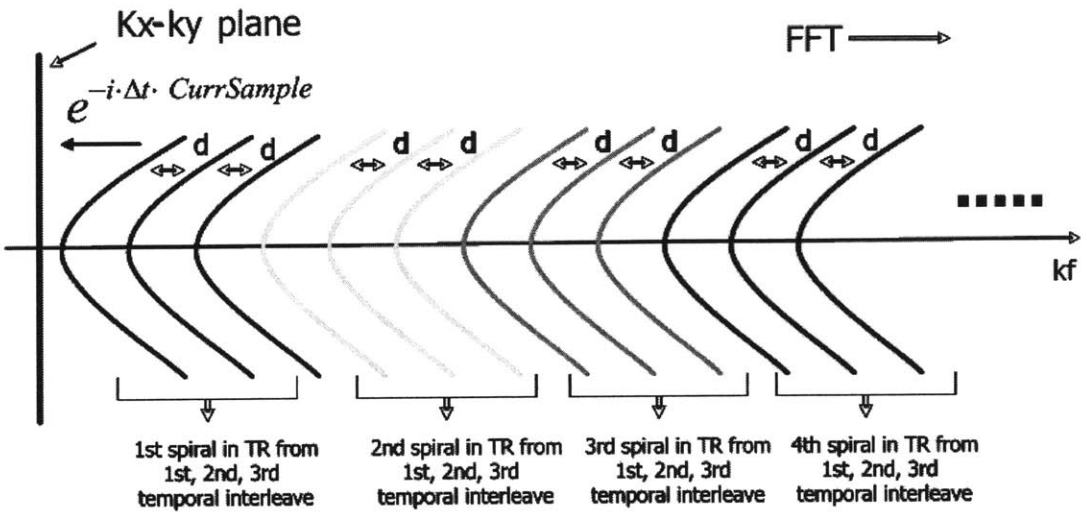

Figure 3-4: Schematic explanation of the improvement of the gridding algorithm based on the fact that samples along k_f axis are sampled uniformly. After appropriately rearranging the samples from all the temporal and angular interleaves, they are appropriately phased and FFT along the k_f axis is performed. The resulting (k_x, k_y, f) matrix is gridded along k_x and k_y axis only, to obtain the desired (x,y,f) data.

Lastly, the (k_x, k_y, f) data that has just been obtained is non-uniformly sampled only along k_x and k_y directions. Performing gridding along these two dimensions will give us the desired (x, y, f) space sampled on Cartesian grid. Figure 3-4 shows a graphical description of the whole process. Looking at this picture, one can think about this improvement as projecting samples along the k_f axis onto the $k_x k_y$ plane followed by a 2D gridding routine.

Implementing this technique to the reconstruction program (written in C programming language) for the *in vivo* experiments was not pursued at the current time, as the entire reconstruction program is being transferred to the online Siemens' Image Calculation Environment (ICE). However, MATLAB routines were written in order to experimentally verify the proposed concept. For this task 2-dimensional (encoding in k_x, k_y, k_f) spiral CSI scans were performed on a spectroscopic spherical phantom.

Figure 3-5a and Figure 3-5b show the end results of the regular (3D gridding) and the enhanced (FFT along k_f followed by 2D gridding) reconstruction routine, respectively.

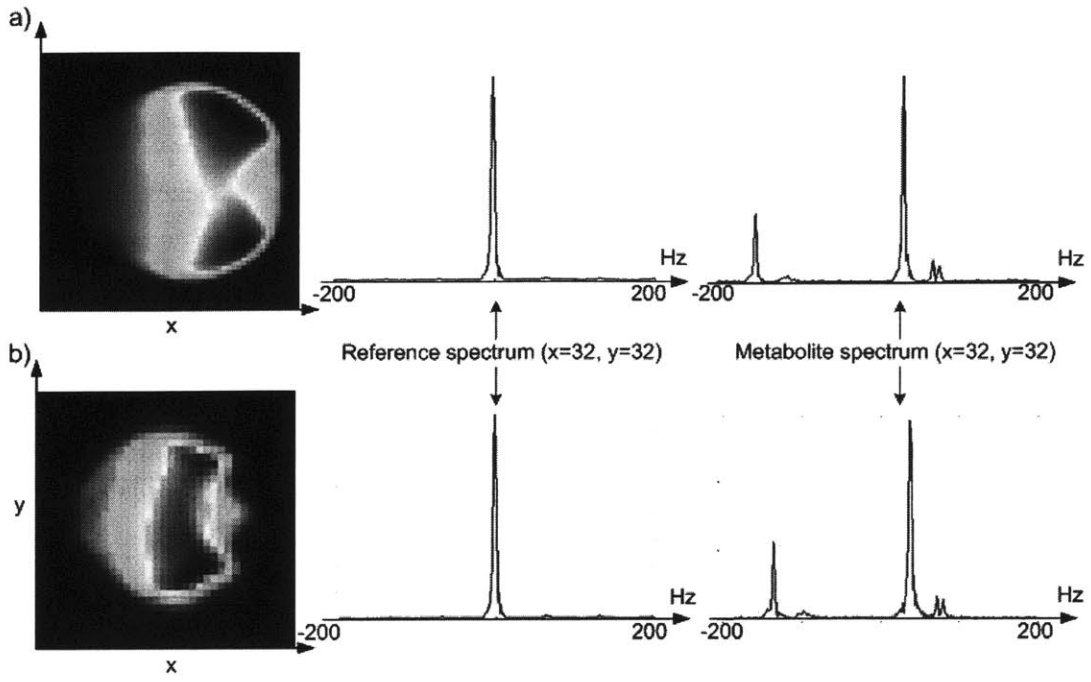

Figure 3-5: Image data over all frequencies, reference spectrum and metabolite spectrum at (x=32,y=32) obtained from: a) 3D gridding reconstruction; b) 1D FFT along k_f axis followed by 2D gridding along k_x and k_y directions.

Note that both the reference and metabolite spectra in this figure match quite well. The in-plane (x, y) image data shown on the left, obtained by summing over all frequencies for each value of x and y, however, are different, due to the in-plane data Hanning windowing (Figure 3-5a).

3.2.3 Results from single coil reconstruction

In order to avoid dealing with immense amount of data in the process of debugging the Spiral CSI algorithm, the initial scans were performed on healthy individuals using Siemens 4-channel coil array. Spectra (their real part) from 9 spatial locations of the 16th and 17th slice from the coil that was closest to the back of the subject's head (all shown on the same scale), are shown in Figure 3-6. As it can be seen (and explained in details

in the next section), the real part of the metabolites' peaks are all positive and in phase, guaranteeing coherent complex summation of the spectra from different coils in the process of multi coil reconstruction.

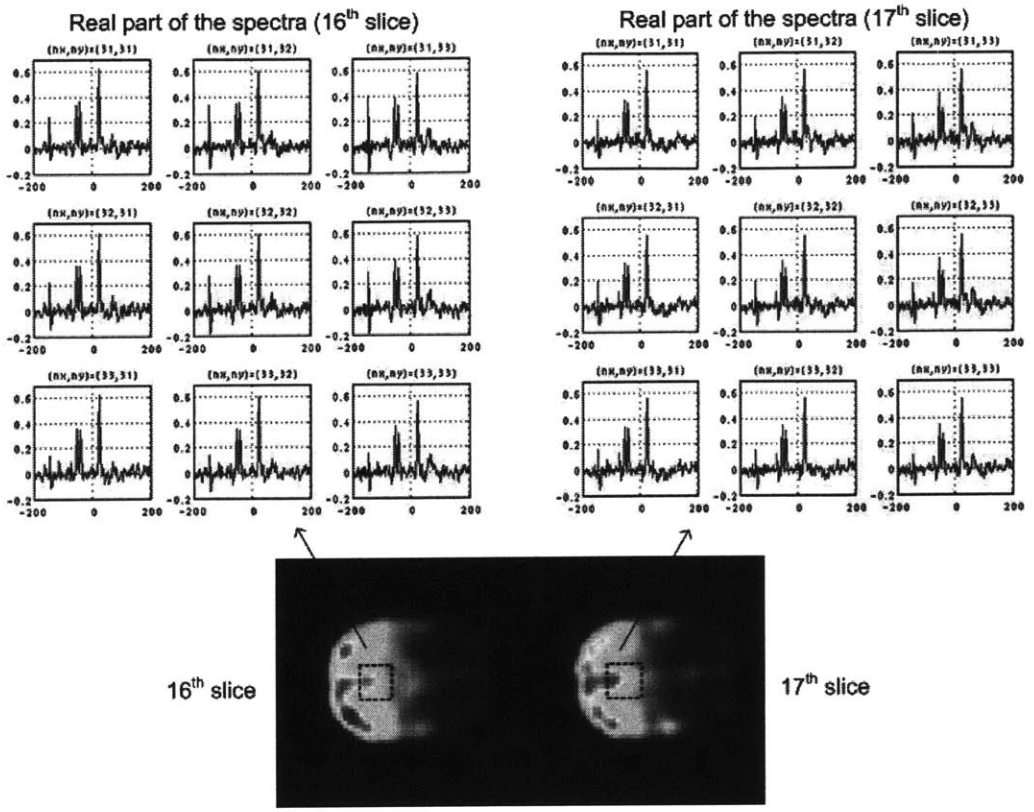

Figure 3-6: Results from reconstruction the data from single coil acquisition. Real parts of the spectra (all shown on the same scale) from the 16th and 17th slice, at nine spatial locations within the specified box are shown. TI/TE/TR=N/A/288ms/2s.

Table 2: SNR measures from the spectra shown on Figure 3-6

SNR measures	x=31	x=32	x=33
y=31, z=16	24.7813	25.1850	26.8451
y=32, z=16	22.7338	24.6160	27.0143
y=33, z=16	19.6610	21.4282	23.2798
z=17, y=31	23.2249	23.2814	25.3988
z=17, y=32	22.5909	24.2582	27.5131
z=17, y=33	21.5778	23.6747	26.8834

A measure of how well the algorithm did was obtained by calculating the SNR for spectra at each spatial location. A way to measure the SNR in MRSI is given by:

$$SNR \simeq \frac{A_{NAA}}{\sigma_N} \tag{3.11}$$

where A_{NAA} is the measured area under the NAA peak and σ_N is the standard deviation of the noise. Whereas obtaining the value of the former is trivial, calculating the latter requires some extra work involving estimation of the noise level. An estimate of the noise distribution at given (x, y) point is obtained by subtracting the reconstructed spectrum from its linear least square fit, which tries to estimate the measured peaks for NAA, Cre and Cho as exponential functions in a linear least square sense using MATLAB's LLSE capabilities. After estimating the noise function, σ_N was determined numerically. Table 2 shows the SNR measure of the spectra shown on Figure 3-6.

3.2.4 Phasing of the reconstructed data

Since the acquisition time used is rather long (400ms), it is desired to collect signal for a longer portion of the FID. This is achieved by turning on the ADC immediately after the Spatial-Spectral 180 degree flip RF pulse, such that the effective spin echo will happen somewhere in the middle of the FID. Although this insures larger portion of the signal recorded to be useful (which is critical in the Spiral CSI), it introduces some post-processing that needs to be done on the reconstructed data. Since, by definition, the time of the effective spin echo is the time where all the spins are rephased, and since the signal in a TR period is recorded before the TE, all the complex spectra from all the (x, y, z) locations have a linear phase term that needs to be corrected for. In order to correct for this linear phase, one would multiply all the spectra with a linear phase term, such that the new spectrum at every pixel is

$$s_{corr}(f) = s_{orig}(f) \cdot e^{j \cdot 2 \cdot \pi \cdot t_0 \cdot f} \tag{3.12}$$

for all values of x, y and z and for some value of the constant t_0. Using the reconstructed gridded data, for TE=288 ms, the value for t_0 was estimated as described

below. Note that, changing either the TE time or the number of samples along the f axis (e.g. 512 instead of 256) would change the value of t_0.

The exact value of t_0 was estimated in a two-step process: firstly, a range of t_0 values that would roughly shift the TE peak of the time signal back to the time origin was defined; secondly, fine tuning to find the exact value was done by looping over the defined range of values and choosing t_0 such that the real part of all the metabolites' spectra were positive and even functions, and their imaginary parts were odd functions. This ensured the metabolites signals to be in phase, which was critical to the multi-coil reconstruction: when doing complex weighted sum of spectra from certain spatial positions from different coils, it is important that these spectra are adding coherently, therefore producing results that maintain optimal SNR. The plots showing the real part of the spectra in Figure 3-6 are example of appropriately performed phase correction.

Having corrected for the linear phase, however, is not the only correction that was to be done. For proper multi-coil reconstruction, one would also need to account for spatial frequency shifts. These shifts are mainly due to B_0 inhomogeneities as a function of spatial locations. In other words, depending on where in the excited region we are, different pixels might have slightly different value of what they consider to be the central frequency. In order to determine what these frequency offsets are, one would find the peak of the spectrum of the reference scan (which has one, large-in-SNR, water peak) for every pixels and consider that to be the central frequency for that particular spatial position. If the frequency value of the reference spectrum peak is denoted by f_0, then the Fourier transform of the spectrum *at each spatial position* is corrected as:

$$d_{corr}(t) = d_{orig}(t) \cdot e^{i \cdot 2 \cdot \pi \cdot f_0 \cdot t} \tag{3.13}$$

where $d_{corr}(t)$ is the Fourier transform of $s_{corr}(t)$.

Frequency drift corrections are important for accurate generation of metabolite and reference (water) spatial maps. Why is this the case is left for the later section in this chapter that talks more about how these maps are being created.

Having implemented the linear phase and frequency shift corrections guarantees coherent reconstruction using multi channel coil arrays. The next section will address the

process of appropriately combining the data from different coils in order to produce results that have SNR improvement over the single coil data shown above.

3.3 Multi coil reconstruction

The basic motivation behind multi coil reconstruction is the SNR improvement over a single coil sensitive to the entire volume. Given a receive coil array composed of coils that are mostly sensitive to only portion of the space, spectra only at these spatial locations will have significantly good SNR. Further, if some spatial locations are in the sensitive regions of two or more coils, adding the signal from these coils can theoretically improve the SNR even further. However, spatial locations further away from the coil's most sensitive region will suffer from low SNR, suggesting that combining the data from all coils by performing simple complex summation over all the (x, y, z) positions, is suboptimal.

An intuitive way to combine the data from many coils is to use *weighted* complex sum [47]. Given a spatial location (x_0, y_0, z_0), the spectra from coils C_i and C_j will be multiplied with the weights w_i and w_j, respectively in a way that the value of w_i will be small if (x_0, y_0, z_0) is away from the sensitive region of C_i and the value of w_j will be large if (x_0, y_0, z_0) is inside the sensitive region of C_j. Therefore, for every single pixel in the (x, y, z) space, the combined spectra can be obtained in the following manner:

$$s_{comb}(x_0, y_0, z_0, f) = \frac{\sum_{i=1}^{N_c} w_i \cdot s_i(x_0, y_0, z_0, f)}{\sqrt{\sum_{i=1}^{N_c} w_i^2}} \tag{3.14}$$

where w_i is the appropriate weight from coil C_i, N_c is the number of coils used, and the term in the numerator is a normalization factor that corrects for image non-uniformity.

Initially, spiral CSI scans were performed on 4-channel Siemens Head Matrix Coil Array, for the purposes of easier debugging of the reconstruction process. Figure 3-6 shows spectra from one of these four coils. However, a 23-chanell custom made coil

array from A.A. Martinos Center for Biomedical Imaging (L. Wald, MGH Research Center) was used to perform the final scans.

3.3.1 Coil sensitivities

Regular 3DFT-encoded GRE sequence was used to estimate the coil profiles which directly determine the weights w_i's. It was critical that the slice thickness and location parameters used in this GRE sequence match the ones from the Spiral CSI scan for proper multi coil reconstruction. For a resolution of $N_x/N_y/N_z$ = 64/64/32pixels, FOV_{xy}/FOV_z = 24cm/12cm, and TR = 100ms, this scan lasted for a little longer than three and a half minutes, and it was done as the last scan in the scanning session.

The figures on the left-hand side in Figure 3-7a,b show profiles obtained by direct reconstruction of the GRE acquisition from the 4, and 23 channel arrays, respectively. Looking at these images, one can easily argue that they posses information not only about the coil sensitivity, but also about the anatomical structure of the subject's head. The w_i's in (3.14), however, are meant to reflect only the coil sensitivities. That is why some post-processing of the current GRE maps has to be done.

Moreover, these maps can be *roughly* thought of as a superposition of two signals, a high frequency one, reflecting the anatomical structure, and a low frequency one, reflecting the coil sensitivity. Therefore, a way to get rid of the anatomical information is to apply an aggressive low pass filter on the current profiles. Although this method will do the desired smoothing, some portions of the head will still posses some anatomical information.

Another way to estimate the coil sensitivities is to find the linear least square estimate for all the slices of the GRE scan. Essentially, the estimate for a given slice is a 2D plane oriented (tilted) in a way that the error between the slice and the its fit is minimized in a linear least square sense. Note that now, these estimate have no anatomical information. However, they are a suboptimal estimate solution for the true coil sensitivities, since they are only first order (linear) estimates. These estimates were used to determine the w_i's in (3.14). They are shown on the right-hand side of Figure 3-7a,b for the case of 4 and 23 channel coil array, respectively. As a note, the number above each of the images represents the absolute scaling of certain profile relative to all

the others, and is obtained by dividing its maximum valued by the maximum value of all the profiles.

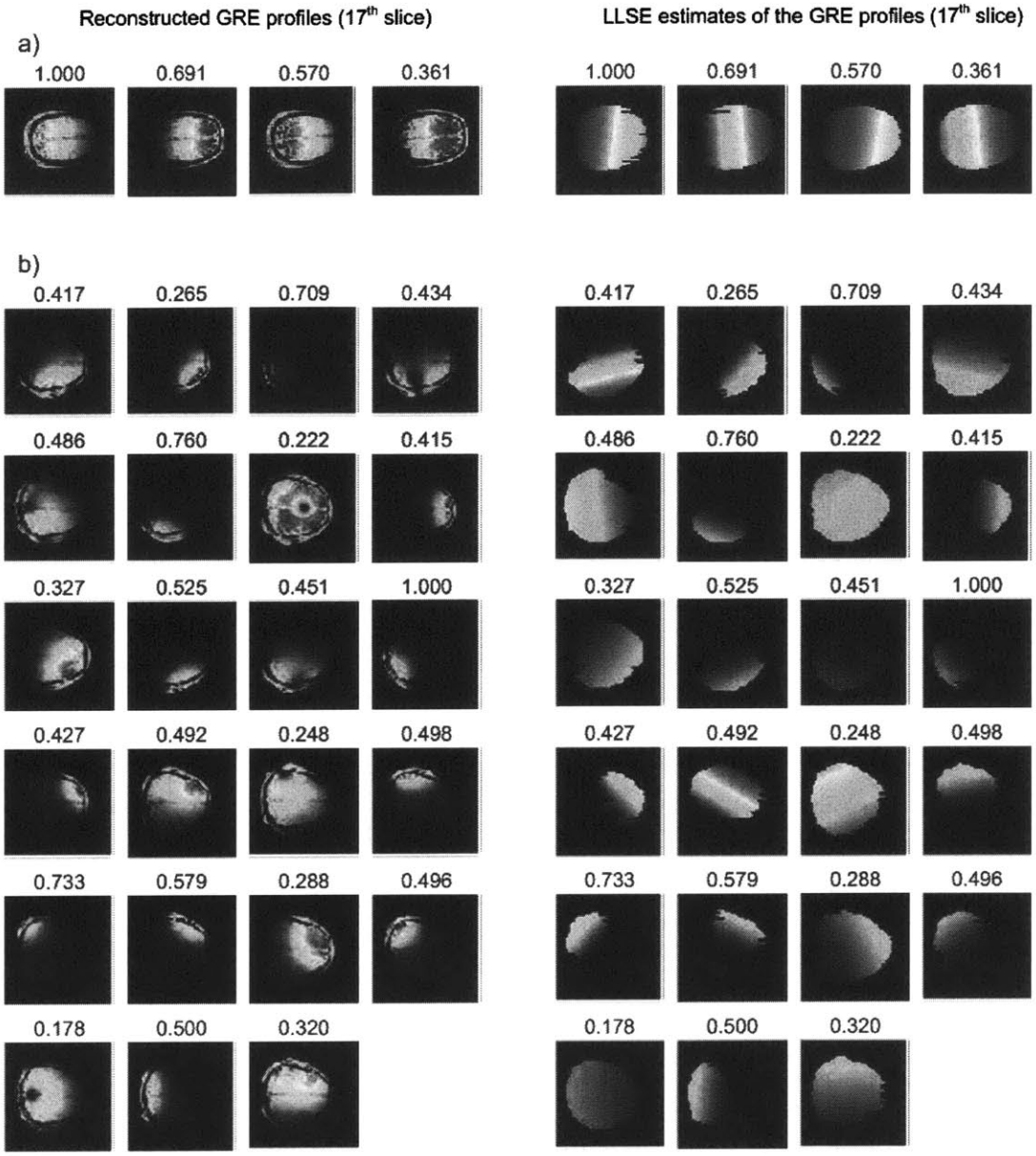

Figure 3-7: Reconstructed GRE profiles (left-hand side) and their LLSE estimate (right-hand side) for the 17th slice (magnitude plots); a) 4-channel coil array; b) 23-channel coil array. The numbers above each image represent the absolute scaling of the profile relative to the rest of the profiles. For example, in b) the maximum value among all the profiles is in the 12th coil, which is twice as large as the maximum value in the 22nd coil.

Having obtained the 3-dimensional matrix holding the coil sensitivity estimates, the real and positive w_i's in (3.14) were found in a three-step process (for each 3D coil data individually) that includes: 1. taking the absolute value of the coil's 64x64x32 data matrix; 2. finding the maximum value in this matrix; 3. Dividing the matrix by the maximum value so that the values are all ranging from 0 to 1, giving the values of the weights for every spatial location and for every coil. At this stage everything is prepared to perform the multi-coil reconstruction

3.3.2 Results: Spectra and measured SNR

Here I present some spectra and measured SNR. Figure 3-8 and Figure 3-9 show plots of the real part of spectra from 9 spatial locations in the xy plane (16th and 17th slice) of the combined data set from 4-channel and 23-channel acquisition, respectively.

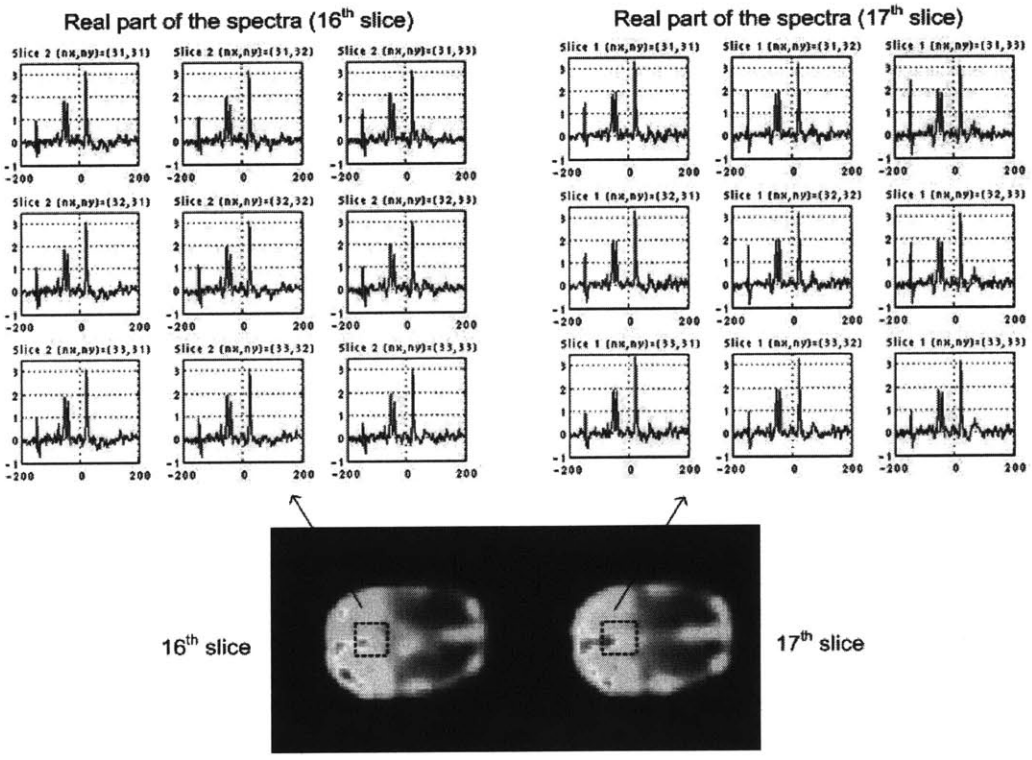

Figure 3-8: Results from reconstruction the combined data from 4-channel coil array acquisition. Real parts of the spectra (all shown on the same scale) from the 16th and 17th slice, at nine spatial locations within the specified box are shown. TI/TE/TR=N/A/288ms/2s.

Table 3: SNR values for the spectra shown in Figure 3-8.

SNR measures	x=31	x=32	x=33
z=16, y=31	28.0731	27.6691	29.1061
z=16, y=32	25.3059	26.4946	29.0895
z=16, y=33	21.7677	23.6410	26.3395
z=17, y=31	27.2275	26.5702	28.6093
z=17, y=32	26.7905	27.4186	30.3778
z=17, y=33	25.7293	27.2577	30.3474

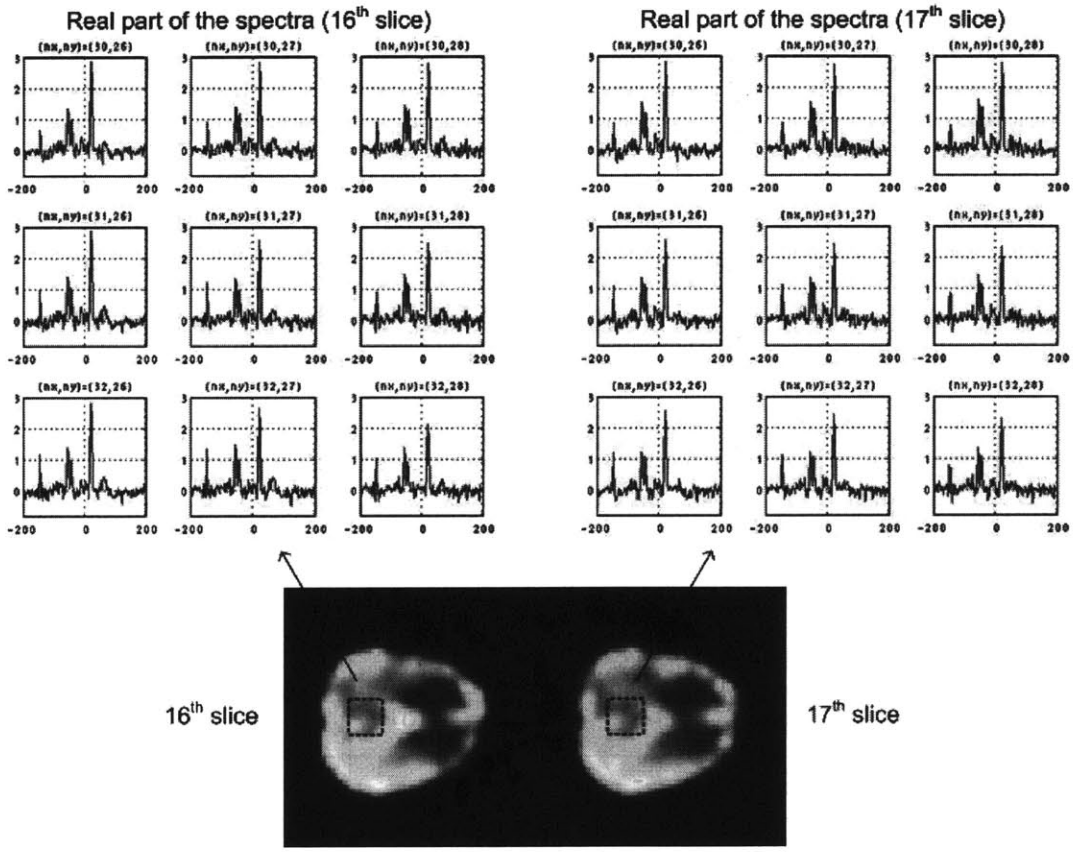

Figure 3-9: Results from reconstruction the combined data from 23-channel coil array acquisition. Real parts of the spectra (all shown on the same scale) from the 16th and 17th slice, at nine spatial locations within the specified box are shown. TI/TE/TR=N/A/288ms/2s.

Table 4: SNR values for the spectra shown in Figure 3-9

SNR measures	x=31	x=32	x=33
Z=16, y=31	30.0040	30.7288	31.7332
Z=16, y=32	28.0664	29.7664	30.0875
Z=16, y=33	23.2859	25.6839	27.4422
Z=17, y=31	29.5864	29.7429	30.3158
Z=17, y=32	31.5986	31.1459	30.6685
Z=17, y=33	30.1170	30.5834	30.7871

Using the methods for calculating the SNR explained in Section 3.2.3, Table 3 and Table 4 show SNR values for the spectra shown in Figure 3-8 and Figure 3-9, respectively.

Firstly, looking at the numerical values in Table 2 (Section 3.2.3) and Table 3 one can immediately observe the SNR improvement, expected when going from single to multi-coil acquisition. This result is comforting and agrees with the theoretical predictions. For convenience, Table 5 shows the SNR ratios obtained by dividing the SNR measures in Table 3 by those in Table 2 for each spatial location.

Table 5: SNR ratios between the single and 4-channel reconstruction. The value in this table for a specific spatial location is obtained by dividing the SNR measures in Table 3 by those in Table 2.

SNR ratios	x=31	x=32	x=33
z=16, y=31	1.1328	1.0986	1.0842
z=16, y=32	1.1131	1.0763	1.0768
z=16, y=33	1.1072	1.1033	1.1314
z=17, y=31	1.1723	1.1413	1.1264
z=17, y=32	1.1859	1.1303	1.1041
z=17, y=33	1.1924	1.1513	1.1289

Moving to the results for the 23-channel acquisition (Table 4), although the SNR values are higher compared to the 4-channel acquisition (Table 3), it must be noted that the spatial positions at which the SNR is measured do not exactly coincide. The reason is simple: the subject had to get out of the scanner so that the coil arrays can be changed. Therefore, we did our best to experimentally (trial-and error approach) match these 18 spatial positions of interest, having in mind that perfect match will never be possible. However, the spatial location from Figure 3-6 and Figure 3-8 match exactly, and the presented SNR improvement is what matters the most.

The last topic in this chapter will be presenting the metabolites and reference maps, and that is to be discussed next.

3.3.3 Results: Metabolite and Reference maps

Besides the representation of the combined data as shown in Figure 3-7 and Figure 3-9, the spectroscopy society is interested in metabolites maps (images) that show the amount of particular metabolite as a function of space. The maps are obtained by simply integrating the area under the metabolite of interest for all the spatial locations. For example, if the area under the NAA peak at spatial position $(x_{im} = 25, y_{im} = 31)$ is A_{NAA}, the NAA spatial map at position $(x_{map} = 25, y_{map} = 31)$ will be assigned this value.

Obtaining the amount of certain metabolite relies heavily on its chemical shift value, since the estimation routine will calculate the area under the spectrum that is around the chemical shift value for that metabolite. That is why correcting for frequency drifts, discussed in Section 3.2.4 is very critical. For example, let's assume that a spectrum at certain spatial location has frequency drift equivalent to -0.3 ppm due to field inhomogeneities. Now the NAA peak will be positioned at 1.7 ppm, rather than at the true value which is at 2.0 ppm along the frequency axis. Thus, the estimation routine that tries to find the amount of NAA will report value that doesn't reflect the true amount of NAA at that particular spatial location.

Figure 3-10 and Figure 3-11 show metabolite (NAA, Cre and Cho) and reference maps from the 4-channel and 23-channel acquisition. The relative scaling between the maps (clearly indicated above and below a map) is solely for the purpose of better visualization. In addition, all the maps are acquired without any inversion adiabatic pulse

played, due to certain SNR issues experienced during the scans when the adiabatic pulse was turned on (at the present moment, we are in the process of resolving these issues).

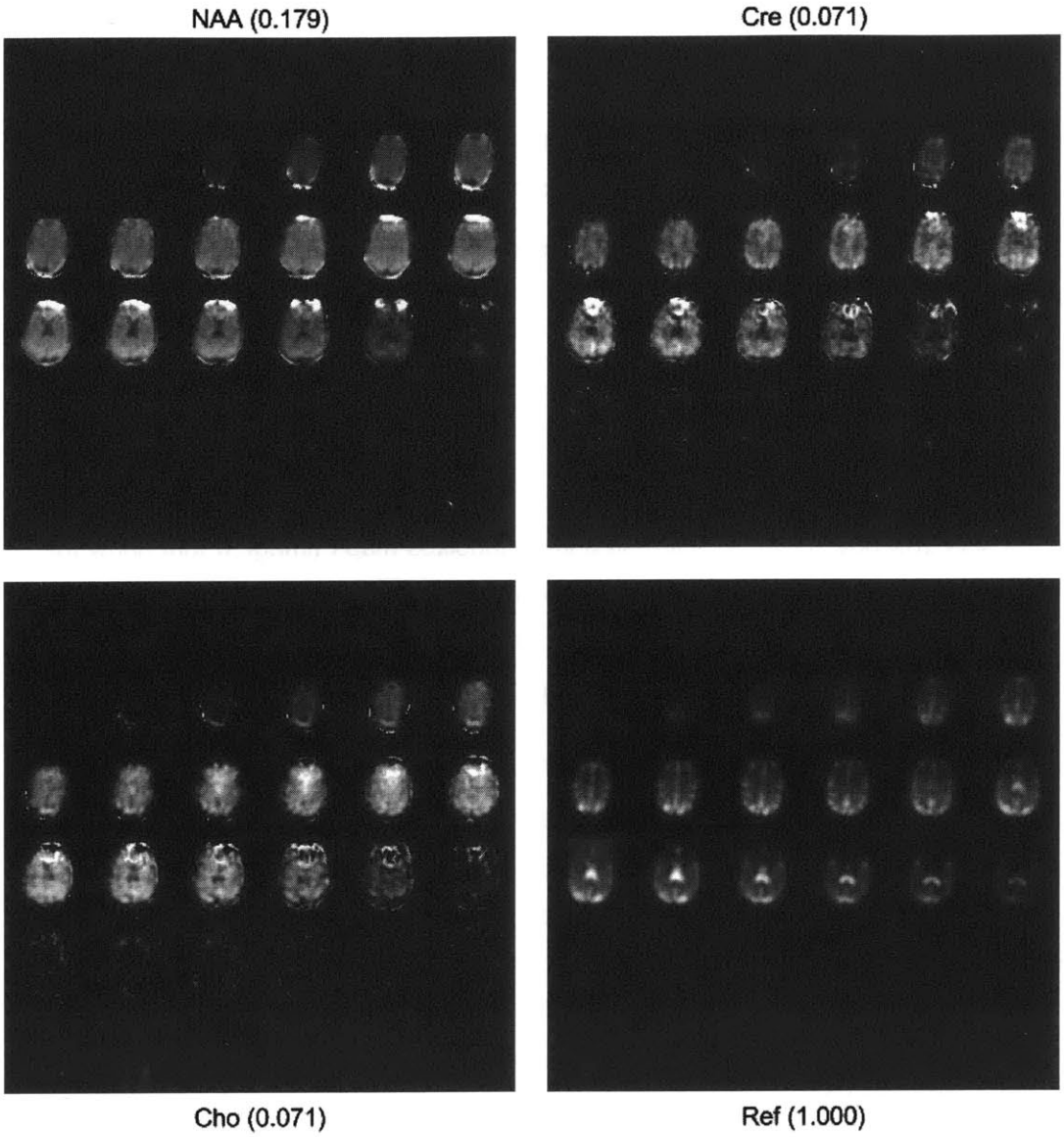

Figure 3-10: NAA, Cre, Cho and on-resonance (water) maps from a 3D volumetric 4-channel acquisition. The first three are obtained from the 15 minutes metabolite scans, whereas the last one is obtained from the 4 minutes reference scan. The numbers shown represent the absolute scaling of a map relative to the rest of the maps.

The absence of the adiabatic pulse can be easily seen on the NAA maps from the 23-channel acquisition due to the fact that most of the coils are sensitive around the

periphery of the head, therefore collecting more of the lipid signal that is around the head. However, once the adiabatic pulse is proved to be working, those saturated regions in all metabolite maps, noticeable in the periphery of the head, will be significantly decreased.

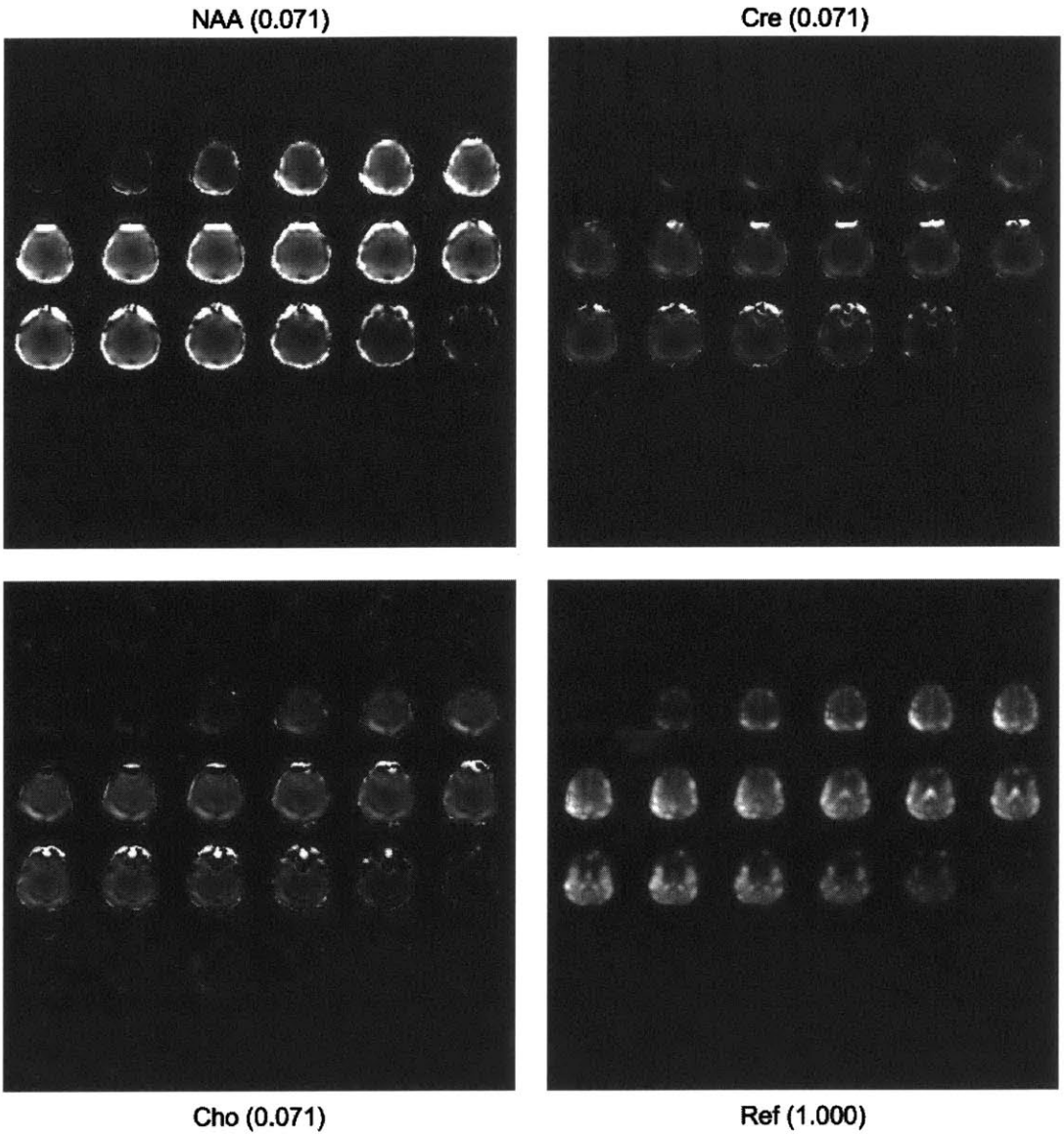

Figure 3-11: NAA, Cre, Cho and on-resonance (water) maps from a 3D volumetric 23-channel acquisition. The first three are obtained from the 15 minutes metabolite scans, whereas the last one is obtained from the 4 minutes reference scan. The numbers shown represent the absolute scaling of a map relative to the rest of the maps.

4 Summary

One of the main motivations for conducting research in the area of MRSI is the ability to obtain physiological information non-invasively. The fundamental challenges in MRSI are the intrinsically low-in-SNR metabolite signals, strong lipid and water resonances and B_0 inhomogeneities. The additional constraint in conventional MRSI is the long acquisition time. The work presented in this thesis joins the many others that try to address and effectively resolve these issues with a hope that spectroscopic imaging will become even faster and more accurate.

4.1 Contributions

The work in this thesis provides the following contributions:

- Implementation of the spiral CSI algorithm on 1.5T Siemens platform.
- Providing a proof of concept that the current reconstruction routine can be made more efficient, by not doing gridding along the directions that are uniformly sampled (k_z and k_f in the current case). The proposed idea suggests that along these dimensions, Fourier transform is done first, followed by some appropriate phase corrections.
- Using multi-coil arrays for acquisition of spectroscopic data sampled in a way prescribed by the spiral CSI algorithm. This implementation yields spectra with higher SNR than single coil acquisitions.

4.2 Future work

The work presented in this thesis will serve as a basis for future work that can extend in several directions.

Although the spiral CSI algorithm reduces the scanning time significantly compared to conventional CSI, further time reduction is possible. For the case of multi-coil acquisitions, parallel imaging techniques (SENSE [48], SMASH [49] or GRAPPA [50] to name a few) make use of sensitivities information embedded in the coils used for the purposes of scanning time reduction. This has drawn major attention in the last years, so the usage of these techniques for structural imaging has recently become common practice. However, parallel spectroscopic imaging has just been recently touched upon, and will gain more attention in the future. The immediate challenge is the SNR loss due to the further reduction of the scanning time – a consequence of doing parallel imaging. Parallel spiral CSI would present a valuable contribution to the field of MRSI.

Two-dimensional spectroscopy, which acquires data along two time dimensions, t_1 and t_2, is a technique that is used for analysis or detection of coupled spin systems [51, 52]. Since in order to acquire spatially resolved 2D spectra the spatial k-space dimensions must be sampled for each t_1, fast spectroscopic imaging makes 2D spectroscopy feasible to obtain in reasonable scanning times. Implementing 2D spectroscopy on the Siemens platform would provide methods for detection and quantification of coupled spins, such as glutamine, glutamate and gaba in an MRSI format.

Finally, one might ask what are optimal ways to traverse a volumetric 3D k-space for the case of spectroscopic imaging given the constrains such as minimal SNR, maximum scanning time, and RF coil array. One possibility is not to phase-encode along the z direction, but rather to play the G_z gradient in the readout. This has the potential to reduce the scanning time at the cost of increasing the complexity of the reconstruction. Also, another interesting way to do spectroscopic imaging is not to sample the entire spatial k-space, but rather only to acquire samples at "the most significant" k-space locations. Finding the k-space coefficients that contribute the most in the process of retrieving the object domain data is an active area in the field of sparse approximation, which is used in source coding or compression applications.

5 Bibliography

1. Bloch, F., *Nuclear Induction.* Physics Review, 1946. **70**: p. 460-473.
2. Purcell, E.M., H.C. Rottery, and R.V. Pound, *Resonance absorption by nuclear magnetic moments in a solid.* Physics Review, 1946. **69**: p. 37-38.
3. Lauterbur, P.C., *Image formation by induced local interactions: Examples employing nuclear magnetic resonance.* Nature, 1973. **242**: p. 190-191.
4. Abragam, A., *Principles of nuclear magnetism.* 1961.
5. Bernstein, M.A., K.F. King, and Z. X.J., *Handbook of MRI Pulse Sequence.* 2004.
6. Ernst, R.R., G. Bodenhausen, and W. A., *Principles of nuclear magnetic resonance in one and two dimensions.* 1987.
7. Nishimura, D.G., *Principles of magnetic resonance imaging.* 1996.
8. Adalsteinsson, E., et al., *Volumetric spectroscopic imaging with spiral-based k-space trajectories.* Magn Reson Med, 1998. **39**(6): p. 889-98.
9. Pan, J.W., et al., *Quantitation of metabolites by 1H NMR.* Magn Reson Med, 1991. **20**(1): p. 48-56.
10. Brown, T.R., B.M. Kincaid, and K. Ugurbil, *NMR chemical shift imaging in three dimensions.* Proc Natl Acad Sci U S A, 1982. **79**(11): p. 3523-6.
11. Howe, F.A., et al., *Proton spectroscopy in vivo.* Magn Reson Q, 1993. **9**(1): p. 31-59.
12. Meyer, C.H., et al., *Simultaneous spatial and spectral selective excitation.* Magn Reson Med, 1990. **15**(2): p. 287-304.
13. Macovski, A., *Noise in MRI.* Magn Reson Med, 1996. **36**(3): p. 494-7.
14. Edelstein, W.A., et al., *The intrinsic signal-to-noise ratio in NMR imaging.* Magn Reson Med, 1986. **3**(4): p. 604-18.
15. Macovski, A., *Volumetric NMR imaging with time-varying gradients.* Magn Reson Med, 1985. **2**(1): p. 29-40.
16. Bowtell, R., M.G. Cawley, and P. Mansfield, *Proton chemical-shift mapping using PREP.* Journal of Magnetic Resonance, 1989. **82**(3): p. 634-639.
17. Doyle, M. and P. Mansfield, *Chemical-shift imaging: a hybrid approach.* Magn Reson Med, 1987. **5**(3): p. 255-61.
18. Haase, A., *Snapshot FLASH MRI. Applications to T1, T2, and chemical-shift imaging.* Magn Reson Med, 1990. **13**(1): p. 77-89.
19. Haase, A. and D. Matthaei, *Spectroscopic FLASH Imaging (SPLASH imaging).* Journal of Magnetic Resonance, 1987. **71**: p. 550-553.
20. Mansfield, P., *Spatial mapping of the chemical shift in NMR.* Magn Reson Med, 1984. **1**(3): p. 370-86.

21. Matsui, S., K. Sekihara, and H. Kohno, *High-speed spatially resolved NMR spectroscopy using phase-modulated spin-echo trains. Expansion of the spectral bandwidth by combined use of delayed spin-echo trains.* Journal of Magnetic Resonance, 1985. **64**: p. 161-171.

22. Matsui, S., K. Sekihara, and H. Kohno, *High-speed spatially resolved high-resolution NMR spectroscopy.* Journal of the American Chemical Society, 1985. **107**: p. 2817-2818.

23. Twieg, D.B., *Acquisition and accuracy in rapid NMR imaging methods.* Magn Reson Med, 1985. **2**(5): p. 437-52.

24. Twieg, D.B., *Multiple-output chemical shift imaging (MOCSI): a practical technique for rapid spectroscopic imaging.* Magn Reson Med, 1989. **12**(1): p. 64-73.

25. Twieg, D.B., J. Katz, and R.M. Peshock, *A general treatment of NMR imaging with chemical shifts and motion.* Magn Reson Med, 1987. **5**(1): p. 32-46.

26. Webb, P., D. Spielman, and A. Macovski, *A fast spectroscopic imaging method using a blipped phase encode gradient.* Magn Reson Med, 1989. **12**(3): p. 306-15.

27. Adalsteinsson, E. and P. Irarrazabal, *Spectroscopic magnetic resonance imaging using spiral trajectories* 1997, The Board of Trustees of the Leland Stanford Junior University (Palo Alto, CA) USA.

28. Brooker, H.R., T.H. Mareci, and J.T. Mao, *Selective Fourier transform localization.* Magn Reson Med, 1987. **5**(5): p. 417-33.

29. Parker, D.L., G.T. Gullberg, and P.R. Frederick, *Gibbs artifact removal in magnetic resonance imaging.* Med Phys, 1987. **14**(4): p. 640-5.

30. Mareci, T. and B. HR, *High-resolution magnetic resonance spectra from a sensitive region defined with pulsed field gradients.* Journal of Magnetic Resonance, 1984. **57**: p. 157-163.

31. Adalsteinsson, E., et al., *Reduced Spatial Sidelobes in Chemical-Shift Imaging with Variable-Density Spiral Trajectories*, in *International Society of Magnetic Resonance in Medicine*. 1998. p. 361.

32. Zur, Y., *Design of improved spectral-spatial pulses for routine clinical use.* Magn Reson Med, 2000. **43**(3): p. 410-20.

33. Schick, F., *Simultaneous highly selective MR water and fat imaging using a simple new type of spectral-spatial excitation.* Magn Reson Med, 1998. **40**(2): p. 194-202.

34. Block, W., et al., *Consistent fat suppression with compensated spectral-spatial pulses.* Magn Reson Med, 1997. **38**(2): p. 198-206.

35. Pauly, J.M., D.G. Nishimura, and A. Macovski, *A k-space analysis of small-tip-angle excitation.* J. Magn Reson., 1989. **81**(1): p. 43-56.

36. Conolly, S., et al., *Variable-rate selective excitation.* J. Magn Reson., 1988. **78**: p. 440-458.

37. Hardy, C.J., W.A. Edelstein, and D. Vatis, *Efficient adiabatic fast passage for NMR population-inversion in the presence of radiofrequency field inhomogeneity and frequency offsets.* J. Magn Reson., 1986. **66**: p. 470-482.

38. Rosenfeld, D. and Y. Zur, *A new adiabatic inversion pulse.* Magn Reson Med, 1996. **36**: p. 124-136.

39. Silver, M.S., R.I. Joseph, and D.I. Hoult, *Highly selective pi/2 and pi pulse generation.* J. Magn Reson., 1984. **59**: p. 347-351.

40. Spielman, D.M., et al., *Lipid-suppressed single- and multisection proton spectroscopic imaging of the human brain.* J Magn Reson Imaging, 1992. **2**(3): p. 253-62.

41. Alley, M.T., G.H. Glover, and N.J. Pelc, *Gradient characterization using a Fourier-transform technique.* Magn Reson Med, 1998. **39**(4): p. 581-7.

42. O'Sullivan, J.D., *A fast sinc function gridding algorithm for Fourier inversion in computer tomography.* IEEE Trans. Med. Imag., 1985. **4**(4): p. 200-2007.

43. Meyer, C.H., et al., *Fast spiral coronary artery imaging.* Magn Reson Med, 1992. **28**(2): p. 202-13.

44. Irarrazabal, P., et al., *Spatially resolved and localized real-time velocity distribution.* Magn Reson Med, 1993. **30**(2): p. 207-12.

45. Jackson, J.I., et al., *Selection of a Convolution Function for Fourier Inversion using Gridding.* IEEE Transactions on Medical Imaging, 1991. **10**(3): p. 473-478.

46. Beatty, P.J., D.G. Nishimura, and J.M. Pauly, *Rapid gridding reconstruction with a minimal oversampling ratio.* IEEE Trans Med Imaging, 2005. **24**(6): p. 799-808.

47. Wright, S.M. and L.L. Wald, *Theory and application of array coils in MR spectroscopy.* NMR Biomed, 1997. **10**(8): p. 394-410.

48. Pruessmann, K.P., et al., *SENSE: sensitivity encoding for fast MRI.* Magn Reson Med, 1999. **42**(5): p. 952-62.

49. Sodickson, D.K. and W.J. Manning, *Simultaneous acquisition of spatial harmonics (SMASH): fast imaging with radiofrequency coil arrays.* Magn Reson Med, 1997. **38**(4): p. 591-603.

50. Griswold, M.A., et al., *Generalized autocalibrating partially parallel acquisitions (GRAPPA).* Magn Reson Med, 2002. **47**(6): p. 1202-10.

51. Adalsteinsson, E. and D.M. Spielman, *Spatially Resolved Two-Dimensional Spectroscopy*, in *International Society of Magnetic Resonance in Medicine*. 1996. p. 1222.

52. Adalsteinsson, E. and D.M. Spielman, *Spatially resolved two-dimensional spectroscopy.* Magn Reson Med, 1999. **41**(1): p. 8-12.